Table of Contents

List of Figures

Chapter 1

Strongly Correlated Electronic System

1.1 Introduction

In transition-metal oxides, the Coulomb interaction between electrons is of importance for understanding metal-insulator transitions and other properties such as high-temperature superconductivity and colossal magnetoresistance (CMR) [1, 2]. The strong connections among charge, lattice, orbital, and spin degrees of freedom closely related to these phenomena. For example, charge carriers of some novel oxides exhibiting spatial localization on certain sites can result in a metal-to-insulator transition in response to the change of temperature [3]. Figure 1.1 illustrates charge, orbital, and spin orderings of transition-metal oxides. Several types of antiferromagnetic order give rise to a variety of physical phenomena such as the magnetoelectric effect in multiferroics [4, 5]. Spin order also couples with the periodic arrangement of the shape of electron clouds [6], i.e., orbital ordering to which the CMR phenomenon is the most relevant [7]. Therefore, elucidating the nature of charge, orbital, and

spin ordering related to phase transitions is one of the most important subjects in condensed-matter physics.
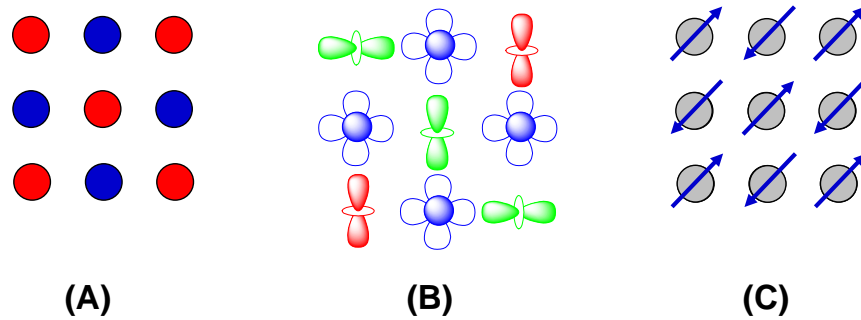
Figure 1.1: Illustrations of charge (A), orbital (B), and spin ordering (C).

1.2   Mott-Hubbard Insulator

Band theory predicts that an insulating state only exists when the bands are fully empty or occupied, otherwise a metallic state. In contrast, many insulators are with charge-orbital partial filled electronic state. A Mott insulating state can occur even the valence band is partially occupied. The reason is that the kinetic energy of electrons is small and their conduction is blocked by the strong Coulomb interaction. For example, in an one-dimensional half-filled system with two $3d$ electrons, as shown in Fig. 1.2, the band theory predicts the system to be metallic. In fact, the Coulomb repulsion reduces the probability of electron hopping and the system can exhibit an insulating behavior, if the on-site Coulomb energy U is larger than the bandwidth. If one electron jumps from site j to site i, the total energy will increase by U due to
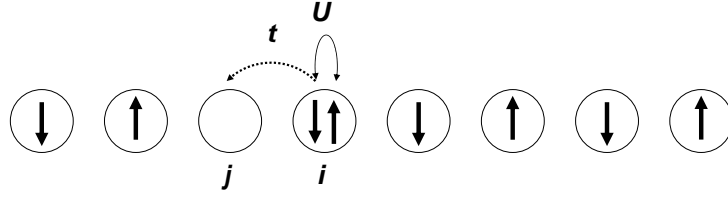
Figure 1.2: A simple 1D electron system with an antiferromagnetic coupling.

the Coulomb interaction. If the U is much larger than t, such a hopping will cause much energy and the material is an insulator of the Mott-Hubbard type [9]. In such a case, the electron-electron interaction is

$$H_U = \frac{1}{2} \sum_\sigma \langle n, n| \frac{e^2}{|r_1 - r_2|} |n, n\rangle c_{n,\sigma}^\dagger c_{n,-\sigma}^\dagger c_{n,-\sigma} c_{n,\sigma} = U n_{i\uparrow} n_{i\downarrow}, \qquad (1.1)$$

where σ is spin quantum numbers (in this case the $S = \pm\frac{1}{2}$); $n_{n\sigma} = c_{n\sigma}^\dagger c_{n\sigma}$. Because of Pauli exclusion principle, the spins of electrons at the same site are different (one spin up and another spin down). In the Hubbard model, the Hamiltonian is

$$H = -t \sum_{\langle ij\rangle\sigma} (c_{i,\sigma}^\dagger c_{j,\sigma} + h.c.) + U \sum_i n_{i\uparrow} n_{i\downarrow}, \qquad (1.2)$$

where t is the hopping integral of electrons between two neighboring transition ions. For $U \gg t$, electrons are localized on every site in the ground state. It is unfavorable for two electrons on the same site.

1.3 Jahn-Teller Distortion

In transition-metal oxides with the perovskite structure, the $3d$ transition metal ion is surrounded by six oxygens ion, as shown in Fig. 1.3 (A). Due to the crystal-field

effects, the $3d$ bands split into an e_g doublet and a t_{2g} triplet degeneracy. The lobes of orbital directed to the ligands are of e_g orbitals, and those of orbital directed to the direction between two ligands are of t_{2g} orbitals. The degeneracy of e_g and t_{2g} orbitals can be lifted due to the orbital-lattice interaction called the Jahn-Teller effect. For example, when the oxygens in z axis move toward or away from the transition metal ion, the local symmetry is broken and the e_g-orbital degeneracy splits into the $d_{x^2-y^2}$ and $d_{3z^2-r^2}$ orbitals. Because the strong hybridization with ligands, e_g electrons have a strong JT effect. However, for the t_{2g} orbital, the orbital degeneracy is associated with the weaker π-bonding. Therefore the energy splitting of t_{2g} orbital is less than that of e_g orbital. The d_{yz} and d_{zx} orbitals are still degenerate by symmetry. Only d_{xy} orbital will have a different energy. The Jahn-Teller effect thus reduces the total energy. For example, as shown in Fig. 1.3 (B), a distortion in which the oxygen ions in the $\pm z$ direction move away from the transition metal ion and the others in the x and y direction move closer will make the energy of $d_{x^2-y^2}$ orbital higher than that of $d_{3z^2-r^2}$ orbital. For Mn^{3+}, there are four electrons in the $3d$ energy band, three in the t_{2g} and the other in the e_g. The energy of $d_{3z^2-r^2}$ orbital with the Jahn-Teller effect is reduced. In addition, the cooperative Jahn-Teller effect will cause an orbital order.

1.4   Charge-Orbital Order

For $La_{1-x}Ca_xMnO_3$ with $x = 0.5$, Wollan and Koehler [11] characterized the antiferromagnetic and ferromagnetic patterns by neutron scattering and named the
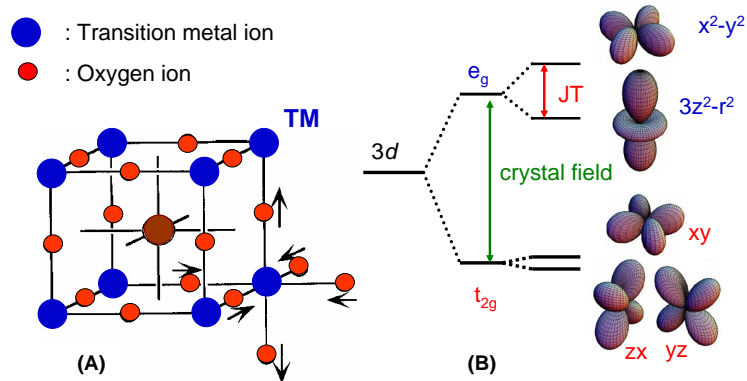
Figure 1.3: (A)Schematic view of a crystal with the cubic perovskite structure. (B)Schematic figure of the 3d band of transition metal ion with an octahedral crystal field and the Jahn-Teller effect.

insulating state as the CE-type antiferromagnetic phase. In the same year, Goodenough [12] proposed the charge-orbital order picture with CE-type AFM applied to a half-doped perovskite-type manganite, where the manganese ions are with Mn^{3+} and Mn^{4+}. Figure 1.4 shows the picture of such charge-orbital order. In the MnO_2 plane below the Neel temperature, there exist ferromagnetic zigzag chains of Mn^{3+} and Mn^{4+} bridged by oxygens with Mn^{4+} situated on the corner sites. The spins between zigzag chains are AFM coupled via the superexcahnge interactions. The ferromagnetic phase is caused by double exchange interaction.
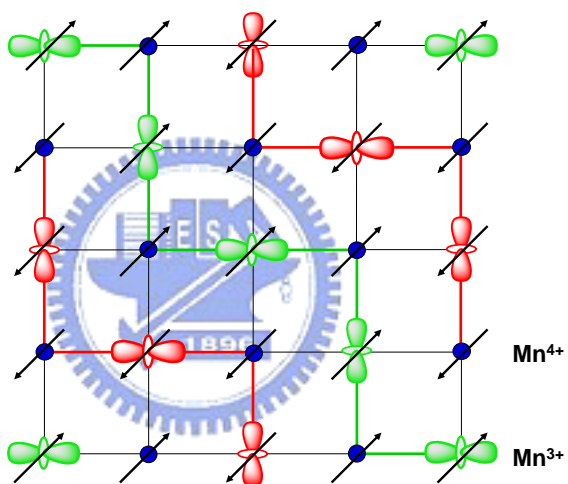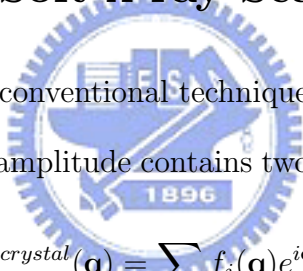
Figure 1.4: Picture of charge-orbital order with CE-type AFM.

Chapter 2

Experimental Techniques and Setup

2.1 Resonant Soft x-ray Scattering

X-ray diffraction is a conventional technique to probe the structure of crystalline material. The scattering amplitude contains two terms, as expressed in the following,

$$F^{crystal}(\mathbf{q}) = \sum_{\mathbf{r}_j} f_j(\mathbf{q}) e^{i\mathbf{q}\cdot\mathbf{r}_j} \sum_{\mathbf{R}_n} e^{i\mathbf{q}\cdot\mathbf{R}_n}, \qquad (2.1)$$

where the first term is the structure factor of unit cell, the second term is a sum over lattice sites; $\mathbf{R}_n$ is the lattice vector, and $\mathbf{r}_j$ is the position of atoms.

Figure 2.1 illustrates the process of resonant scattering. In the resonant condition, the incident photon excites an electron to an excited state. After excitation, the electron then decays back to the initial state by emission a photon. If the energy of incident photon is the same as that of scattered photon, the resonant scattering is elastic. The atomic form factor is

$$f(\mathbf{q}, \hbar\omega) = f^0(\mathbf{q}) + f'(\hbar\omega) + i f''(\hbar\omega) \qquad (2.2)$$
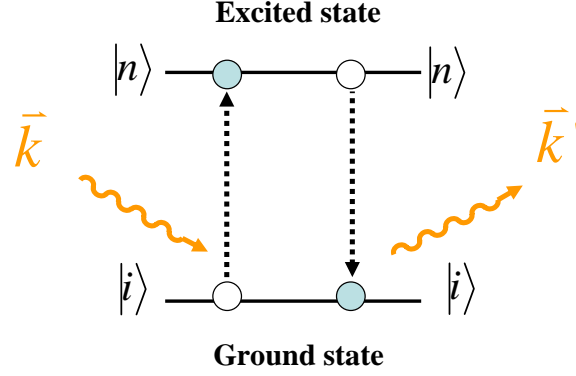
Figure 2.1: Illustration of resonant x-ray scattering.

where f' and f'' are the real and imaginary parts of the dispersion corrections to f^0. The f' and f'' are dominated by tightly bound inner-shell electrons (i.e. electrons in the K, L, and M shell) and can not have any appreciable dependence on $\mathbf{q}$. On the other hand, $f^0(\mathbf{q}) \propto -Zr_0$ for small $\mathbf{q}$, known as Thomson scattering, is independence of photon energy, but related to the scattering vector $\mathbf{q}$. In some symmetric conditions or the low cross-section scattering condition, $f^0(\mathbf{q})$ nearly goes to zero. From equation 2.2, when the photon energy is equal to one of the absorption edge of the atom, f' and f'' will enhance dramatically manifesting the element specific characteristics. For example, the cross section of magnetic scattering is smaller than x-ray charge scattering by $(\hbar\omega/mc^2)^2 \sim 10^{-6}$ [13]. Detection of magnetic order with off-resonant scattering is difficult against a strong background fluorescence. Beside, for neutron scattering technique [14, 15, 16], the cross section of magnetic order is much larger than that of the x-ray scattering as discussed in Appendix A. It is difficult to detect the magnetic order by x-ray scattering, By using resonant scattering, the cross section

of magnetic scattering is dramatically enhanced [17]. The transition between the core

levels with spin-orbit splitting and empty states with exchange splitting is sensitive

for magnetic order.

Considering the electrons in a quantized electromagnetic field, the Hamiltonian is

given by [13]

$$H = \sum_j \frac{1}{2m}(\mathbf{P}_j - \frac{e}{c}\mathbf{A}(\mathbf{r}_j))^2 + \sum_{ij} V(r_{ij}) - \frac{e\hbar}{mc} \sum_j \mathbf{s}_j \cdot \bigtriangledown \times \mathbf{A}(\mathbf{r}_j)$$

$$+\frac{e\hbar}{2(mc)^2} \sum_j \mathbf{s}_j \cdot [\mathbf{E}(\mathbf{r}_j) \times (\mathbf{P}_j - \frac{e}{c}\mathbf{A}(\mathbf{r}_j))] + \sum_{k\lambda} \hbar\omega_k(\mathbf{a}_{k\lambda}^\dagger \mathbf{a}_{k\lambda} + \frac{1}{2}), \qquad (2.3)$$

where the vector potential, $\mathbf{A}(\mathbf{r}) = \sum_{\lambda k} \sqrt{\frac{2\pi\hbar c^2}{V\omega_k}}[\hat{e}_{\lambda k}\mathbf{a}_{\lambda k}e^{i\mathbf{k}\cdot\mathbf{r}} + \hat{e}_{\lambda k}^*\mathbf{a}_{\lambda k}^\dagger e^{-i\mathbf{k}\cdot\mathbf{r}}]$, is linear

in creation and annihilation operators $\mathbf{a}_{\lambda k}^\dagger$ and $\mathbf{a}_{\lambda k}$. For electrons in a quantized

electromagnetic field, the Hamiltonian can be divided to H_0, H_{rad}, and H_{int}. The

interaction term (H_{int}) is due to the interaction between the photon and the electron,

the Hamiltonian can be described by

$$H_{\mathrm{int}} = \sum_j \frac{e}{2mc^2}\mathbf{A}^2(\mathbf{r}_j)^2 - \sum_j \frac{e}{mc}\mathbf{A}(\mathbf{r}_j) \cdot \mathbf{P}_j - \frac{e\hbar}{mc} \sum_j \mathbf{s}_j \cdot [\bigtriangledown \times \mathbf{A}(\mathbf{r}_j)]$$

$$-\frac{e^2}{c^2}\frac{e\hbar}{2(mc)^2} \sum_j \mathbf{s}_j \cdot [\frac{\partial \mathbf{A}}{\partial t} \times \mathbf{A}(\mathbf{r}_j)], \qquad (2.4)$$

In the second-order perturbation theory, the transition probability is given by the

"Fermi golden rule"

$$W = \frac{2\pi}{\hbar}|\langle f|H_{\mathrm{int}}|i\rangle + \sum_n \frac{\langle f|H_{\mathrm{int}}|n\rangle\langle n|H_{\mathrm{int}}|i\rangle}{E_i - E_n}|^2\rho(E_f), \qquad (2.5)$$

where $|i\rangle$, $|f\rangle$, and $\rho(E_f)$ are the initial, final states, and density of state, respectively.

The first term is dominated in non-resonant scattering regime, the cross section would

be

$$(\frac{d^2\sigma}{d\Omega'dE'}) = (\frac{e^2}{mc^2})^2 \{\langle f| \sum_j e^{i\mathbf{q}\cdot\mathbf{r}_j}|i\rangle \epsilon' \cdot \epsilon - i\frac{\hbar\omega}{mc^2}\langle f| \sum_j e^{i\mathbf{q}\cdot\mathbf{r}_j}\mathbf{s}_j|i\rangle \epsilon' \times \epsilon\}^2, \quad (2.6)$$

The first term of equation 2.6 is the Thomson scattering, and second term depends on the spin density. The cross-section from magnetic order is thus smaller than that from charge order by $(\hbar\omega/mc^2)^2$.

In the resonant scattering regime, the second term of equation 2.5 is enhanced. The ground state $|i\rangle$ is excited by the incident photon to intermediate state with $|n\rangle$. From the second term of equation 2.5, the spin-dependent terms become

$$\frac{\hbar^2 k^2}{m}\sum_{ij}\sum_c \frac{\langle f|(\hat{\mathbf{k}}' \times \epsilon')\mathbf{s}_j e^{-i\mathbf{q}\cdot\mathbf{r}_j}|n\rangle\langle n|(\hat{\mathbf{k}} \times \epsilon)\mathbf{s}_j e^{i\mathbf{q}\cdot\mathbf{r}_j}|i\rangle}{E_i - E_n + \hbar\omega - i\frac{\Gamma_c}{2}}, \quad (2.7)$$

where Γ_c is the lifetime width of the core hole and $\frac{\hbar\omega}{\Gamma_c}$ is in the order of 10^4.

According to Hannon *et al.* paper [18], the scattering amplitude can be given by this formula.

$$f_{E1}^{(res)} = \frac{3}{4}\lambda\{(\mathbf{e}_s^* \cdot \mathbf{e}_i)[F_{1,1}^{(e)} + F_{1,-1}^{(e)}] - i(\mathbf{e}_s^* \times \mathbf{e}_i) \cdot \hat{\mathbf{z}}_J[F_{1,1}^{(e)} - F_{1,-1}^{(e)}]$$

$$+ (\mathbf{e}_s^* \cdot \hat{\mathbf{z}}_J)(\mathbf{e}_i \cdot \hat{\mathbf{z}}_J)[2F_{1,0}^{(e)} - F_{1,1}^{(e)} - F_{1,-1}^{(e)}]\}, \quad (2.8)$$

in which $\mathbf{e}_i$ and $\mathbf{e}_s$ are the electric-field vectors of incident and scattered light, respectively, and $\hat{\mathbf{z}}_J$ are the local direction of magnetic order, respectively. $F_{1,q}$ are the scattering amplitudes corresponding to the quantum number q. If the $\mathbf{e}_s^* \times \mathbf{e}_i$ is parallel to the magnetization moment, the scattering cross section form magnetic order would be zero.

In 1998, Murakami *et al.* observed the charge-orbital order with $q = (3/4, 3/4, 0)$ in the single-layered manganites $La_{0.5}Sr_{1.5}MnO_4$ by using resonant x-ray scattering

[19]. For transition metal oxides, the orderings comes from $3d$ electrons. However, this method probes the ordering of $4p$ bands, rather than $3d$ bands. In other words, this scattering technique in the hard x-ray regime is not suitable for probing the ordering of $3d$ states. Resonant L-edge soft-x-ray scattering, on the contrary, is dipole-allowed and sensitive charge-orbital and magnetic order of transition metal compound [20, 21, 22].

2.1.1 Azimuthal-Dependence of Scattering Intensity

Resonant scattering intensity from some specific charge-orbital order shows anisotropy. For instance, the e_g electrons on the Mn^{3+} site in the manganite have an $d_{3z^2-r^2}/d_{x^2-y^2}$ orbital degree of freedom. From the 3rd term of Equation 2.8

$$(\mathbf{e}_s^* \cdot \hat{\mathbf{z}})(\mathbf{e}_i^* \cdot \hat{\mathbf{z}})([2F_{1,0} - F_{1,1} - F_{1,-1}], \tag{2.9}$$

Castleton *et al.* can explain the polarization and azimuthal angle dependence of scattering [24]. The local moment of charge-orbital order $\hat{z}$ along the (100) and (010) direction, the (1/4, 1/4, 0) scattering intensity comes from the difference between f_{E1}^{res} for two Mn^{3+} ions with orbital distribution along $\hat{\mathbf{a}}$ and $\hat{\mathbf{b}}$ direction. Thus, the form factor is proportion to

$$[(\mathbf{e}_s^* \cdot \hat{\mathbf{a}})(\mathbf{e}_i^* \cdot \hat{\mathbf{a}}) - (\mathbf{e}_s^* \cdot \hat{\mathbf{b}})(\mathbf{e}_i^* \cdot \hat{\mathbf{b}})][2F_{1,0} - F_{1,1} - F_{1,-1}], \tag{2.10}$$

For incoming and scattered light, the electric polarization vectors have two kinds, σ and π polarization. The scattering intensity

$$I(\theta, \phi) = \cos^2 \theta \sin^2 \phi [2F_{1,0} - F_{1,1} - F_{1,-1}], \tag{2.11}$$

where θ and ϕ indicate the scattering angle and azimuthal angle, respectively.

2.2 Experimental Setup

2.2.1 The EPU Beamline
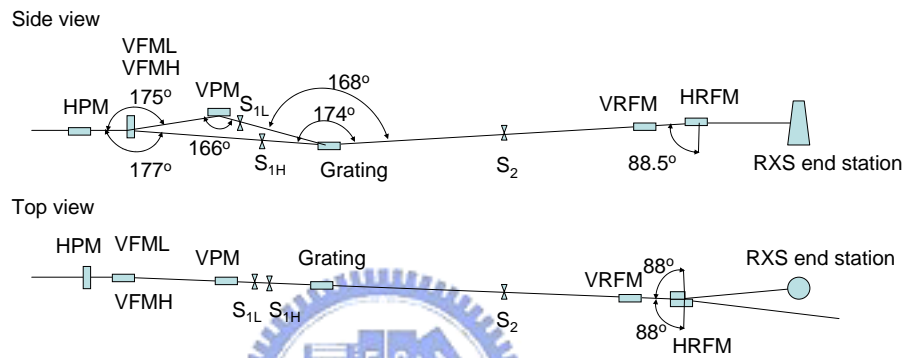
Figure 2.2: Schematic drawing of the EPU beamline.

We measured soft x-ray scattering by using the elliptically polarized undulator beamline (EPU) [25, 26] at National Synchrotron Radiation Research Center (NSRRC), as shown in Fig. 2.2. With this insertion device, the polarized incident light can be adjusted to be either elliptically, circularly polarized, or linearly polarized. There are several key components at this beamline. First, two optics, the horizontal plane mirror (HPM) and the vertical focusing mirror (VFM), independently focus the synchrotron light in the horizontal and vertical direction, respectively. The energy of x-rays was selected through the entrance slit (S_1), the grating, and the exit slit (S_2). To optimize the flux and energy resolution, we typically used a grating ruling of 900 lines/mm for the oxygen K-edge measurements and of 1600 lines/mm

for measurements with energies around $600 \sim 1200$ eV. The exit slit is moveable to increase the resolving power. Typically, we chosed the width of 20 μm for both slits. The monochromatic beam after S_2 was refocused in horizontal and vertical directions by bendable horizontal and vertical refocusing mirrors (HRFM and VRFM), respectively. The photon energy for the Mn L-edge measurements is 0.14 eV if the width of both S_2 and S_2 is set to be 20 μm. A two-circle soft-x-ray diffractometer is situated at the end of EPU beamline.
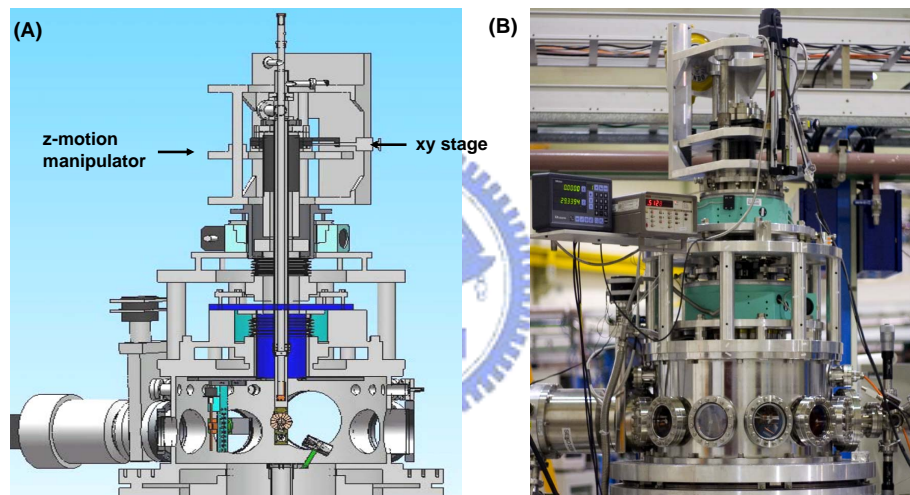
Figure 2.3: Illustration (A) and picture (B) of the two-circle diffractometer.

2.2.2   The UHV Diffractometer

Figure 2.3 presets a photo and a three-dimensional view of the two-circle diffractometer. The sample holder and the detector are inside a UHV chamber. The typical vacuum pressure is the range of 10^{-9} torr without backout. The diffractometer chamber is a cylindrical vessel with an internal diameter of 609 mm. The scattering

geometry is shown in Fig. 2.4. Two rotation stages for an independent rotations of sample (θ) and detector (2θ) are concentrically mounted on the cylinder axis. We use the Huber 420 and 430 as the θ and 2θ goniometers; they are separately coupled to differentially pumped rotary seals. Figure 2.5 (A) shows the combination of the goniometer (Huber 430) and an 8 inch rotary seal, as indicated by red arrows. This setup can rotate the detector in vacuum by Huber 430.
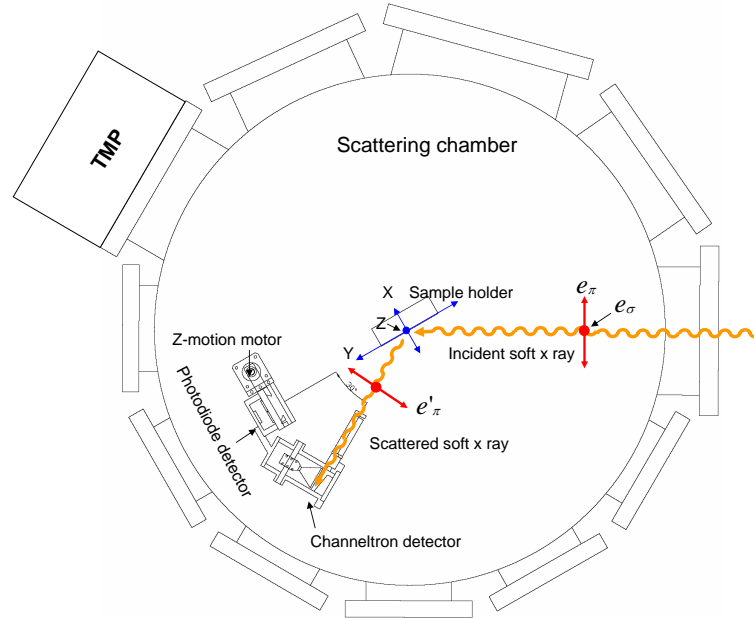
Figure 2.4: Top view of scattering geometry.

Before mounting the sample holder in the two-circle diffractometer, we character-ized its orientation by conventional x-ray diffraction using a four-circle diffractometer to ensure the momentum transfer $\mathbf{q}$ to be measured is in the scattering plane. We adjusted the sample position in the scattering plane by an xy translational stage and the sample height by a z-motion manipulator, as shown in Fig. 2.3 (A) and 2.4. As
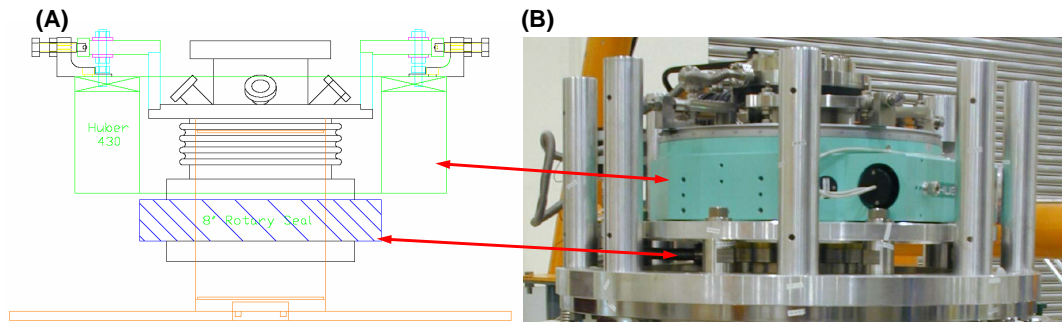
Figure 2.5: Illustration (A) and picture (B) of the goniometer and the differential seal. Red arrows indicate the corresponding parts between these two graphs.

beginning of the experiment, we adjusted the soft-x-ray beam to pass through the axis of θ and 2θ rotations. We located the sample surface to be at the center of the rotation axis. To further check the centering of the sample surface, we rotated the sample by 180°, and then checked if the beam intensity after the sample rotating remains unchanged. If not, we adjusted the beam position (without adjusting the holder) to compensate the offset, and checked the alignment again. After the sample position being centered in the xy plane, i.e., the scattering plane, the sample height was aligned and its orientation was rocked about the nominal zero with the photodiode detector at the position of $2\theta = 0°$. When the sample is properly aligned and the light impinges at the center of sample, the θ rocking curve shows a triangular profile peaked at $\theta = 0°$.

2.2.3   Detector and Electronics

The scattered beam was detected by a silicon p-n junction photodiode or a channeltron detector depending upon the intensity, as shown in Fig. 2.6. For the photodiode

detection, a slit of 0.5-mm width(or 4 mm depending on measurements) was used. The distance between the photodiode and the sample is 195 mm. A vacuum compatible stepping motor was incorporated to offset the vertical tilt of the sample orientation. The travel distance of the detector in the z direction is 50 mm upward or downward. When the photodiode intercepts the scattered beam, the output current from the diode is fed into a current amplifier (Keithley 6512) which generates a voltage signal of analog. In order to achieve a statistical average, we used a voltage-to-frequency converter which has a digital output recorded by a counter. In addition, we obtained the relative photon flux by recording a mesh current I_0 before the diffractometer.

Channeltron   Photodiode
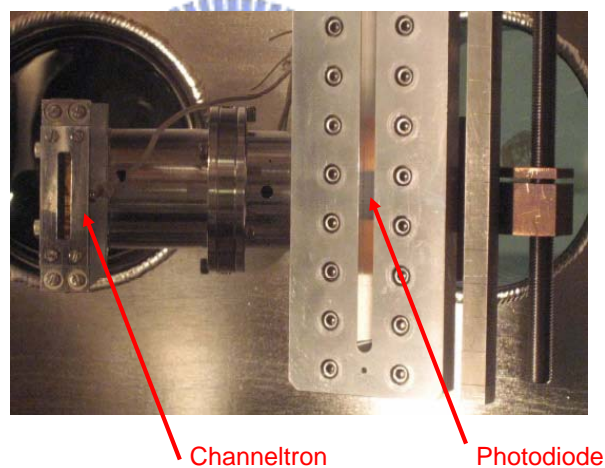
Figure 2.6: Picture of the photodiode and the channeltron detectors.

In addition to the photodiode, a channel electron multiplier (channeltron) incorporated with a CsI thin film for detecting was developed, being used for detecting scattered light of low intensity, as shown in Fig. 2.6. The slit of 1.5-mm width and a mesh were set in front of the channeltron detector. The distance between the channeltron slit and the sample is 171 mm. We applied a biasing voltage from -600 ~

-1200 V on the mesh to eliminate emitted electrons from the sample, depending on the photon energy of incident light. Figure 2.7 is an illustration of the channeltron detector and the block diagram of the electronics for data acquisition. The scattered light hits the CsI film, then generates numerous number of secondary electrons which are eventually collected by the channeltron. The output signal of the channeltron was detected by electronics in a pulse-counting mode. The plus signals were first amplified by a preamplifier, and then separated from electronic noises through a discriminator. Through the level adaptor to stretch the signal pulse width, finally the signals were recorded by a counter.
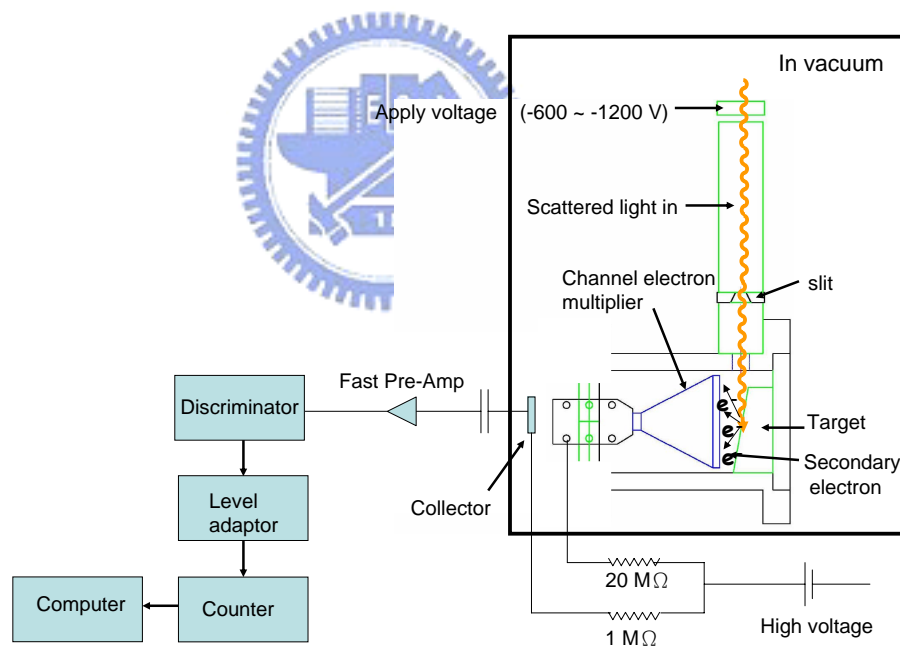
Figure 2.7: Illustration of channeltron detector and block diagram of data acquisition.
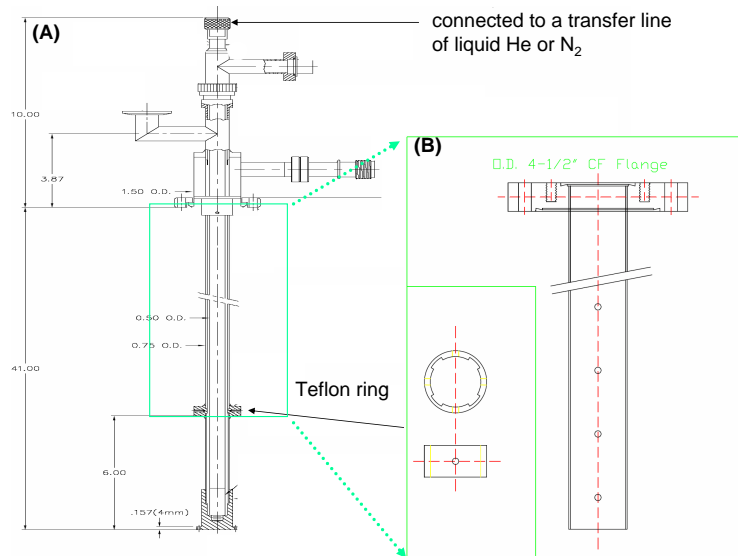
Figure 2.8: Illustration of the cryostat (A) and tube for guiding and thermal shielding (B). The inset of graph (B): Teflon ring used as a spacer between the cryostat and the guiding tube.

2.2.4 Sample Manipulator

For low temperature measurements ($< 340K$), we used an open cycle cryostat of liquid helium incorporated with temperature sensor and heater (Janis ST-400 Ultra High Vacuum Systems) to cool the sample and to control the temperature, as shown in Fig 2.8. In order to reduce the tilting of sample orientation caused by thermal contraction, we made a stainless tube for guiding the cryostat, as shown in Fig. 2.8(B). This guiding tube was also used a thermal shield. Between the guiding tube and the cryostat, a teflon ring was used for thermal insolation, as in the inset of Fig 2.8(B).

There are two types of sample holder used in this dissertation work for measurements with and without azimuthal rotation. For the holder with azimuthal rotation, an in-vacuum stepping motor coupled with a gear reduction rotates the azimuthal

angle; copper braids between the cryostat and the sample holder enhances the cooling efficiency. The lowest temperature of the holder with azimuthal rotation was 80 K (130 K) if the cryostat was cooled by liquid helium (nitrogen).

(A)   **(B)**   **(C)**   **(D)**   **(E)**   **(F)**
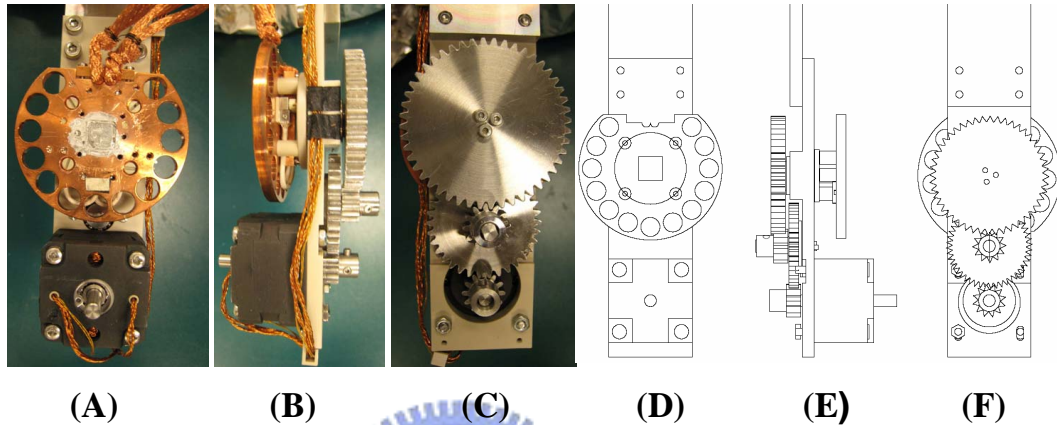
Figure 2.9: Pictures (A)(B)(C) and illustrations (D)(E)(F) of azimuthal rotation. (A) & (D) are the front view of the holder in which the sample was mounted at the middle with four stripes of copper braids for cooling. (B) & (E) and (C) & (F) are the side view and rear view, respectively.

For measurements with temperature below 80 K, we used a sample holder directly connected with cryostat, as shown in Fig. 2.10. This holder can cool down the sample efficiently, and accommodates more than one sample at the same time.
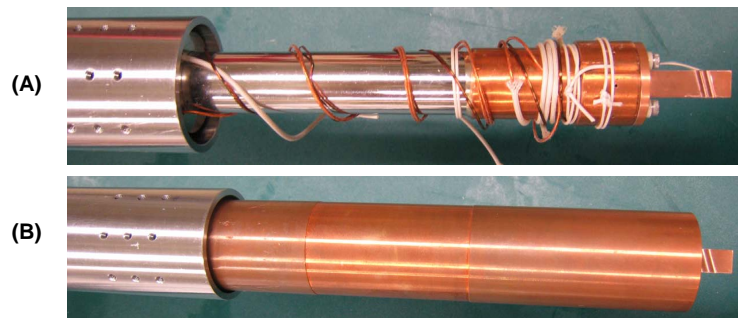
Figure 2.10: Pictures of the sample holder without azimuthal rotation. (A) and (B) are holders with and without a copper thermal shielding.

2.2.5   Software

For motion control and data acquisition, we used a computer software named SPEC to drive the Huber controller through GPIB interface. SPEC is operated under the Linux, a UNIX-based operation system. The SPEC software can scan the angles of the sample and the detector with rotation axes perpendicular to the scattering plane, i.e., θ and 2θ scans. SPEC also provides us momentum scans (q scans) along any direction in the scattering. For energy scan, the computer controls the grating angle via a RS232 interface. For data acquisition, SPEC sets the timer and reads signals from the counter through a CAMAC controller. Not only pulse singles from the channeltron are collected by counters, the current signals from the diode and the mesh are also read by counters through a analog-to-digital conversion scheme described previously (Section 2.2.3).
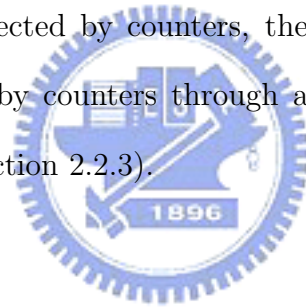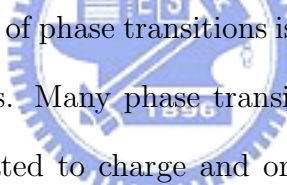
Chapter 3

Charge-Orbital Order in Magnetite

3.1 Fundamental Issues about Magnetite

3.1.1 Verwey Transition

Elucidating the nature of phase transitions is one of the most important subjects in condensed-matter physics. Many phase transitions exhibited by electron-correlated materials are closely related to charge and orbital orderings [2, 1], which manifest themselves in the spatial localization of the charge carriers on certain sites and in the periodic arrangement of specific electron orbitals, respectively. One important example which has fascinated generations of solid-state physicists is the metal-to-insulator transition in magnetite (Fe_3O_4), known as the Verwey transition [28]. Such a transition was first interpreted as a charge order-disorder transition in which the valence electrons order themselves over the octahedral sites (B sites) to form a Fe^{2+} and Fe^{3+} superstructure in the insulating phase [29]. Above the transition temperature (T_V), Fe_3O_4 crystallizes in an inverse spinel structure with a cubic lattice (space group $Fd\bar{3}m, a = b = c = 8.3941$ Å), as shown in Fig. 3.1. Upon cooling through T_V,
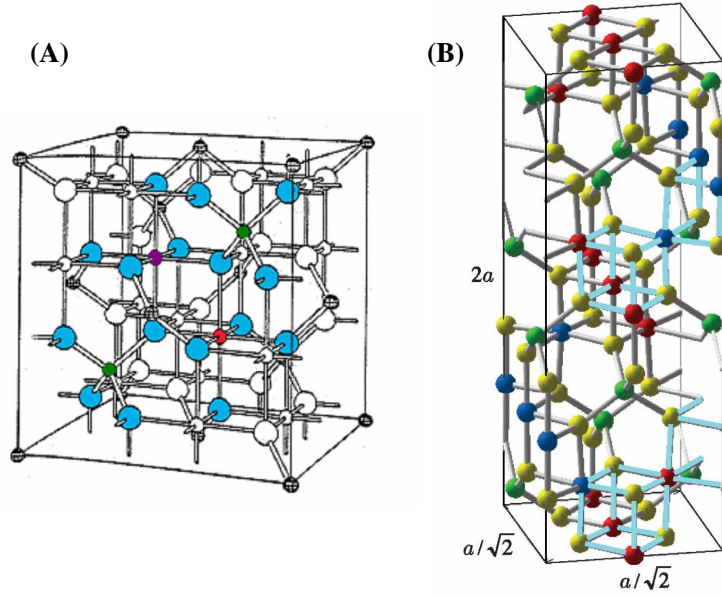
Figure 3.1: (A) Illustration of spinel structure. (B) Monoclinic crystal structure of Fe_3O_4 in the low-temperature phase corresponding to a subcell of $\frac{a}{\sqrt{2}} \times \frac{a}{\sqrt{2}} \times 2a$ with $P2/c$ symmetry. Red (blue), green, and yellow circles indicate B-site Fe^{2+} (Fe^{3+}), A-site Fe^{3+}, and oxygen ions, respectively.

Fe_3O_4 undergoes the Verwey transition in which the electrical conductivity decreases by 2 orders of magnitude, as shown in Fig. 3.2, and the lattice distorts from cubic to monoclinic structure. The low-temperature monoclinic cell (Cc) corresponds to $\sqrt{2}a \times \sqrt{2}a \times 2a$ of the cubic unit cell, consisting of a stacking of eight planes of B sites along the c axis. Manifestations of the Verwey transition also include abrupt changes in magnetic susceptibility and specific heat across the critical temperature. The low-temperature phase of magnetite has been regarded as a classic example of the charge ordering in transition-metal oxides.

On the other hand, electron-phonon interactions [30, 31, 32] have also been attributed to be the driving force of the Verwey transition, as the freezing of phonon modes relieves an instability of the Fermi surface nesting via a mechanism involving
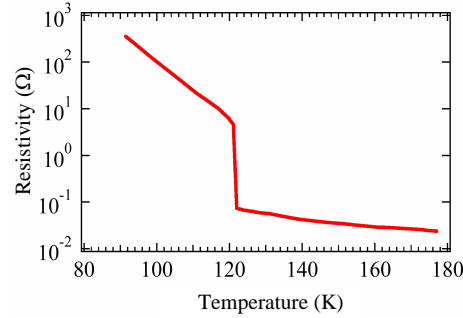
Figure 3.2: Resistance measurement of a Fe_3O_4 single crystal in the vicinity of the Verwey transition.

charge-density waves below T_V, and therefore increases the resistivity.

The mechanism of the Verwey transition is intricate, because neither charge-orbital ordering of valence electrons nor the soft phonon mode has been observed. Many experiments cast strong doubt on the existence of charge ordering in magnetite. In contrast, refinements of x-ray and neutron diffraction [33, 34] suggest the existence of a small charge disproportionation with a modulation vector $q = (0, 0, 1)_c$ and $(0, 0, 1/2)_c$ in units of $2\pi/a$ with a denoting the lattice parameter of the undistorted cubic phase (subscript "c" denotes the high-temperature cubic structure throughout). And charge ordering occurs with a small charge disproportionation, octahedral $Fe^{2.4+}$ and $Fe^{2.6+}$. Such suggestion is supported by LDA + U band-structure calculations which also predict that Fe_3O_4 has a charge-orbital ordered ground state [35, 36]. But this interpretation has been challenged by using resonant x-ray scattering with Fe K-edge. In 2004, Subias et $al.$ concluded the absence of charge ordering with $q = (0, 0, 1)_c$ or $(0, 0, 1/2)_c$ in magnetite [37]. Despite intensive investigations over half a century, the existence of charge ordering in magnetite remains controversial [37, 38, 39, 40, 41]. The mechanism of the Verwey transition is also a yet unresolved

problem.

One main reason for the aforementioned controversy is that experimental technique used in the measurements discussed above are not sensitive enough to provide direct and orbital-sensitive data on the charge-orbital ordering in Fe_3O_4. Among them, resonant x-ray scattering around the Fe K-edge is the most sensitive technique to detect charge-orbital ordering. However, this technique is unable to detect the Fe $3d$ charge ordering directly. Because the Fe $1s \rightarrow 3d$ transition is not dipole-allowed and hence the detection of charge-orbital ordering relies on the hybridization between the Fe $3d$ and Fe $4p$ state and the Fe $1s \rightarrow 4p$ transition. In contrast to Fe K-edge resonant scattering, resonant soft-x-ray scattering around the O K-edge ($1s \rightarrow 2p$) and Fe L-edge ($2p \rightarrow 3d$) are dipole-allowed and can probe the charge-orbital ordering on the Fe $3d$ directly with high sensitivity. The detection of temperature-dependent electronic states across T_V in magnetite is thus a decisive measurement for revealing the mechanism of the Verwey transition.

3.2   Experimental Result

Single crystals of Fe_3O_4 were purchased from Mateck. We performed resonant soft x-ray scattering on single crystals of Fe_3O_4. In order to separate the specular beam and $(0, 0, 1/2)_c$ diffracted beam, we miscut by $3°$ between the sample surface and the $(0, 0, 1)$ crystal surface.

The crystal was fully characterized with x-ray diffraction and was mounted on the sample holder with $(0, 0, 1)$ in the scattering plane, as shown in Fig. 3.3. The e_i and
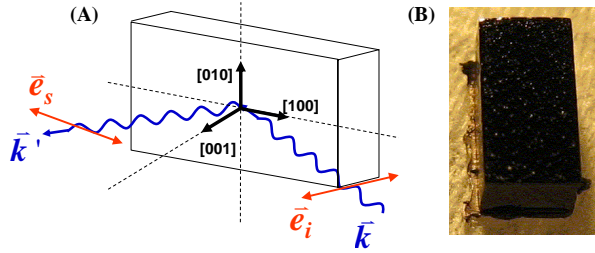
Figure 3.3: (A) Scattering geometry of Fe_3O_4. In charger-orbital-order scattering condition, the polarization of incident and scattered light were the same. (B) Picture of Fe_3O_4 sample.

e_s indicate the electric-field vector of incident and scattered light, respectively. In charger-orbital-order scattering condition, the polarization of incident and scattered light were the same $(\pi \rightarrow \pi', \sigma \rightarrow \sigma')$.

In this section, we show experimental results of ordering of the O $2p$ states and Fe $3d$ states with a modulation vector $(0, 0, 1/2)_c$ at temperature below T_V. Because of the hybridization between the O $2p$ and the Fe $3d$, our finding provides experimental evidence for the existence of charge-orbital ordering in magnetite.

3.2.1 Fe L-edge

The inset of Fig. 3.4 display the intensity of q_z scans through the $(0, 0, 1/2)_c$ peak at various photon energies tune near the Fe L-edge below the Verwey transition. The spectrums with different incident photon energy were vertically offset for clarity. Because of the phase change induced by the real part of the scattering factor, the peak position of the q_z scan slightly deviates from the momentum transfer $q = (0, 0, 1/2)_c$ charge-orbital ordering, as the energy approaches the Fe L_3 edge resonance. Figure 3.4 is the energy dependence of the $(0, 0, 1/2)_c$ superstructure reflection in the vicinity

of Fe L_3 edge of Fe_3O_4 below the Verwey transition. The $(0,0,1/2)_c$ peak is also
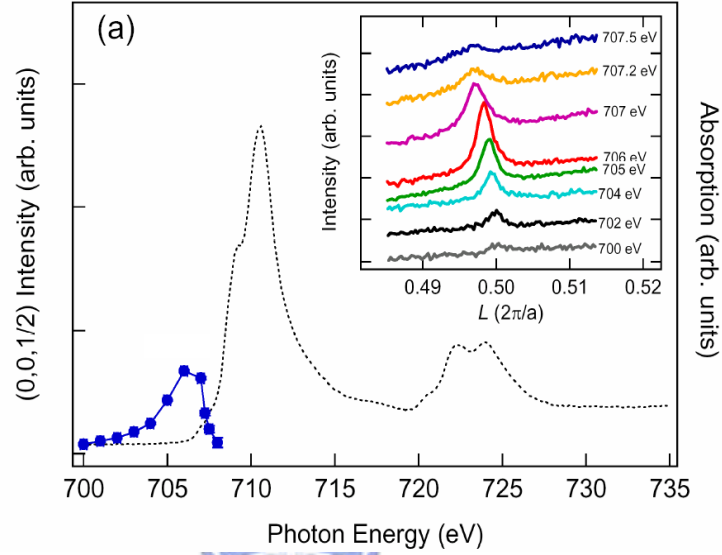
Figure 3.4: Energy dependence of the $(0,0,1/2)_c$ superstructure reflection in the vicinity of Fe L_3 edge of Fe_3O_4 compared with the soft x-ray spectra below the Verwey transition temperature. The inset display the intensity of q_z scans through the $(0,0,1/2)_c$ peak at various photon energies tune near the Fe L-edge.

strongly suppressed with photon energy close to the absorption edge due to the strong self-absorption effect at the Fe L-edge. The observed resonant scattering reveals the charge-orbital ordering Fe $3d$ states [35, 36], in contrast to Fe K-edge resonant scattering [37].

3.2.2   O K-edge

As for the detection of charge ordering in Fe_3O_4, one can employ O K-edge resonant elastic x-ray scattering to examine whether the O $2p$ states exhibit a spatially periodic ordering. Because the O 2p states hybridize with the Fe $3d$ states which are suggested to have a charge ordering with a propagation vector $(0,0,1/2)_c$ [33]. the

intensity $I(\vec{q}, \hbar\omega)$ of resonant soft x-ray scattering with O K-edge is given by [42, 43]

$$I(\vec{q}, \hbar\omega) = | \sum_{Oxygen} e^{iq\cdot r} \int \frac{\rho_{2p}(\varepsilon)d\varepsilon}{\hbar\omega + \varepsilon - E_{1s} - i\Gamma} |^2 \qquad (3.1)$$

where $\hbar\omega$ is the photon energy of incident light; ρ_{2p} is the density of state of O $2p$. The difference in the intensity due to the change of structure factor between photons of energy below and above the O K edge is negligible, i.e.,

$$\frac{| \sum_j (f_{\mathrm{Fe}}e^{iq\cdot r_j} + f_{\mathrm{O}}e^{iq\cdot r_j}) |^2}{| \sum_j (f_{\mathrm{Fe}}e^{iq\cdot r_j} + R \cdot f_{\mathrm{O}}e^{iq\cdot r_j}) |^2} \approx 1 \qquad (3.2)$$

where f_{Fe} and f_{O} are, respectively, the atomic form factors of Fe and O. R is the factor accounting for the enhancement of the form factor of oxygen. In addition, $\vec{q} = (0, 0, 1/2)_c$ and the summation runs over all sites of Fe and O in Fe_3O_4. Therefore, the structure factor of scattering with $\vec{q} = (0, 0, 1/2)_c$ is rather insensitive to the resonance arising from the oxygen atoms in Fe_3O_4; hence the resonant O K-edge scattering with $\vec{q} = (0, 0, 1/2)_c$ can be used to separate the contribution of charge-orbital ordering from the effect of the pure lattice distortion.

Figure 3.5 displays the photon-energy-dependent resonant scattering intensities of Fe_3O_4 around the O K-edge with constant momentum transfer. The data were measured at sample temperature of 80 K with the E vector in the scattering plane and its surface projection along the a axis. Remarkably, the $(0, 0, 1/2)_c$ scattering at energy below the absorption edge (in a narrow energy window from 528.5 to 530.5 eV) enhances dramatically, whereas the scattering intensity is insignificant throughout the absorption white lines (from 530.5 to 536 eV). The observed $(0, 0, 1/2)_c$ resonance scattering is a manifestation of O $2p$ ordering instead of the doubling of the unit
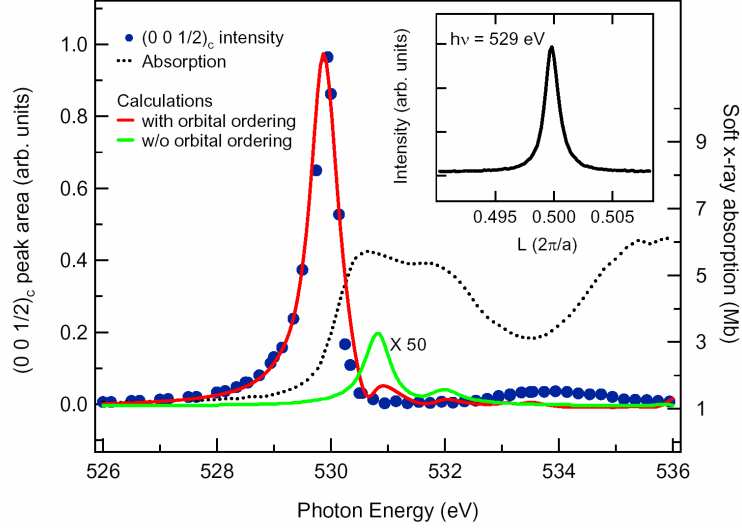
Figure 3.5: Photon-energy dependence of the $(0, 0, 1/2)_c$ scattering intensity (circles) and soft x-ray absorption cross section (dotted line) of Fe_3O_4 around the O K edge ($1s \rightarrow 2p$). The inset displays the q_z scan at photon energy of 529 eV. The scattering measurements are compared with calculated resonant spectrum (solid line).

cell. If the resonant scattering was dominated by a structural effect, the $(0, 0, 1/2)_c$ scattering intensity would be observable both below the O K-edge absorption edge and throughout the absorption white line. In contrast, the ordering of the O $2p$ orbitals with a periodicity of $2a$ will lead to the enhancements of intensity $I(\vec{q}, \hbar\omega)$ of resonant x-ray scattering only at photon energy $\hbar\omega$ corresponding to the excitations of these ordered orbitals and at $q = (0, 0, 1/2)_c$. Our measurements therefore provide evidence for the existence of the superstructure of the ordered O $2p$ orbital states in the vicinity of the Fermi level.

To ensure that the measurements of resonant scattering are not obscured by the self-absorption effect of soft x-ray in the sample, we compared the correlation length ξ of the O $2p$ ordering and the penetration depth of soft x ray. Here we define the

correlation length as $\xi = 2/2\pi(\Delta q)$ with Δq denoting the full width at half maximum of the q_z scan in reciprocal lattice units of $2\pi/a$. The inset of Fig. 3.5 depicts the width of the diffraction peak in the q_z scan at the onset energy of the resonant scattering, giving rise to a correlation length $\xi \sim 900$ Å. Deduced from the measured absorption cross section, the penetration depths of photons with the energy between 528 and 531 eV are greater than 1300 Å, which is larger than the measured correlation length. In the following discussions on the polarization and temperature dependence of O $2p$ ordering, we present data measured with photon energy of 529 eV, at which the penetration depth is 5500 Å, to avoid the experimental complication caused by the sample self-absorption effect. The observed resonance can be an effect of either pure charge modulation or charge-orbital ordering. The latter would lead to a resonant scattering depending on the polarization of the incident soft x ray. With the LDA+U calculations, Guo *et al.* [44] also calculated the resonant x-ray scattering spectrum at the oxygen K edge of Fe_3O_4, as shown in Fig. 3.5. The calculations qualitatively explain the resonance feature of the measured spectrum, further corroborating that the observed resonance arises from the oxygen $2p$ charge-orbital ordering.

In addition, we found that the $(0,0,1/2)_c$ resonant scattering at the O K edge exhibits a polarization dependence. Figure 3.6 shows that the $(0,0,1/2)_c$ scattering spectra taken with the E vector of the incident soft x ray in the scattering plane (E_π) and perpendicular to the scattering plane (E_σ). As the polarization of the soft x ray is rotated from E_π to E_σ, the scattering intensity is reduced.
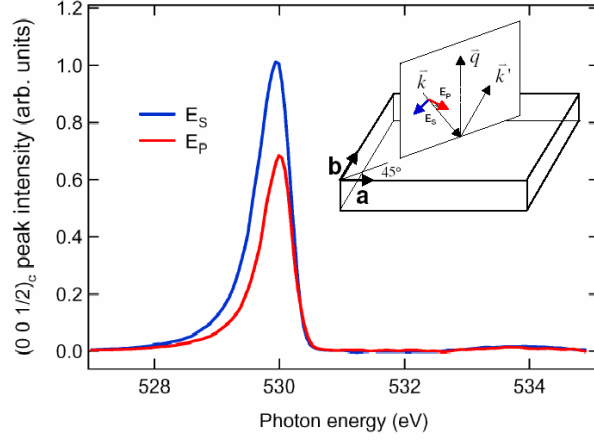
Figure 3.6: Polarization dependence of the $(0, 0, 1/2)_c$ O K-edge scattering intensity. The data were measured at sample temperature of 100 K by using photons with polarization in the scattering plane (E_π) and perpendicular to the scattering plane (E_σ) defined by the incoming wave vector k and the scattered wave vector k', as illustrated in the inset.
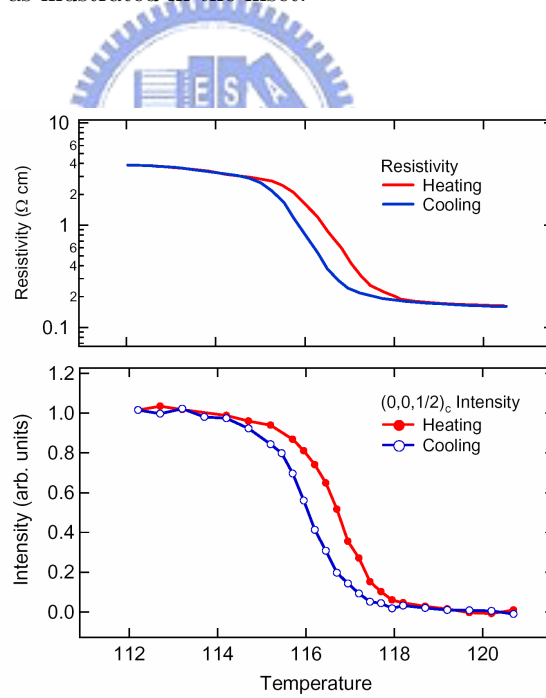
Figure 3.7: Temperature-dependent resistivity (upper panel) and the $(0, 0, 1/2)_c$ O K-edge scattering intensity (lower panel) of Fe_3O_4 across the Verwey transition. The $(0, 0, 1/2)_c$ measurements in heating and the cooling are plotted with connecting solid and dotted lines for visual guidance, respectively. The scattering data were measured with photon energy of 529 eV and with the E vector in the scattering plane and its projection along the a axis.

After experimentally establishing the existence of charge-orbital ordering, we scru-

tinized the nature of the Verwey transition by carrying out temperature-dependent

measurements. The $(0, 0, 1/2)_c$ superstructure peak also exhibits a temperature hys-

teresis that is the characteristic of a first-order transition, similar to the hysteresis of

resistivity. Figure 3.7 displays resistivity and the intensities of the $(0, 0, 1/2)_c$ O K-

edge resonant scattering of Fe_3O_4 measured simultaneously for temperatures across

the Verwey temperature 116.5 K. Upon increasing the temperature and concurrently

with the decrease of resistivity, the scattering intensity decreases abruptly at T_V and

diminishes completely at temperature beyond 119 K, manifesting the disappearance

of charge-orbital ordering at temperature slightly higher than T_V. The O $2p$ states

at the Fermi level contribute to the electric conduction above T_V and undergo a dra-

matic change upon cooling below the Verwey temperature at which these states form

an orbital ordering, opening up an energy gap [35, 36, 45, 46] and thus leading to

the insulating phase. Such charge-orbital ordering is further stabilized by the lattice

distortion.
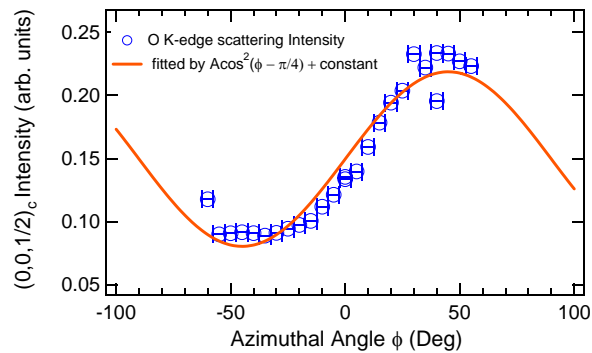
Figure 3.8: Azimuthal-dependent scattering intensity of O K-edge resonant x-ray scattering of $(0, 0, 1/2)_c$ with 529 eV and 80 K.

In addition, we also found the intensity of $(0, 0, 1/2)_c$ exhibits a azimuthal dependence. Figure 3.8 shows the intensity of the charge-orbital order superlattice reflection as a function of the azimuthal angle ϕ. The $(0, 0, 1/2)_c$ peak intensity strongly depends on the azimuthal angle ϕ between the projection of the **E** vector of the incident soft x-ray onto the ab plane. In Fig. 3.8, the azimuthal-dependence scattering intensity follows $\cos^2(\phi - \pi/4)$, showing the two-fold symmetry of the distribution of O $2p$ holes. The error bar is ± 2.5 degree of azimuthal angle from our instrument resolution. However, due to the surface inhomogeneous, the scattering intensity does not reproduce very well. Once rotating the sample, the light hits on the difference site of sample.

To conclude, we found experimental evidence for the charge-orbital ordering in magnetite. O K-edge resonant x-ray scattering reveals that the O $2p$ orbitals in the vicinity of the Fermi level exhibit an ordering with a spatial periodicity of the doubled lattice parameter of the undistorted cubic phase. Our temperature-dependent measurements unravel the electronic nature of the Verwey transition and demonstrate that charge-orbital ordering plays an important role in the Verwey transition of Fe_3O_4, suggesting that the Verwey transition is a transition of charge-orbital ordering.

Chapter 4

Antiferromagnetic order in TbMn$_2$O$_5$

4.1   Introduction of Multiferroelectric

Multiferroics, the coexistence of ferromagnetism and ferroelectrism in materials, being technologically attractive because of the possibility for realizing mutual control of electric and magnetic properties, has recently become the focus of much research in condensed-matter physics. This phenomena was presumed to exist by Pierre Curie [47]. Generally, the induction of a magnetization by means of an electric field or of an electric polarization by means of a magnetic field is referred as the magnetoelectric (ME) effect, which is an important but poorly understood phenomenon [48]. The presence of internal fields could largely enhance the ME effect. However, such enhancement requires the coexistence and strong coupling of magnetism and ferroelectricity (FE), which rarely happen in real materials. The recent discovered coexistence and strong coupling between antiferromagnetism (AFM) and FE in frustrated magnetic materials such as RMnO$_3$ and RMn$_2$O$_5$ (R = Tb, Dy, and

Ho) thus provides new opportunities for exploring mechanism of the enhanced ME effect [49, 50, 51, 52, 53, 54, 55, 56, 57, 59]. In these systems, the spontaneous electric polarization ($\vec{P}$) exhibits in certain AFM phases. Furthermore, experiments [49, 50] demonstrate large changes in $\vec{P}$ by applying external magnetic fields. However, unlike old examples of multiferroics, the magnetic phases involved are complicated and commonly incommensurate (IC) with the lattice. The magnetic transition temperature is higher than the ferroelectric one, suggesting that the ferroelectricity is induced by magnetic order. The inversion symmetry in these phases is broken [57], implying that the magnetic order couples to odd orders of $\vec{P}$. In addition, these materials show nontrivial behaviors in dielectric constants. For $R\text{MnO}_3$, Kenzelmann *et al*. [57] have shown that the multiferroic behavior can be understood by coupling high and low temperature IC magnetic order to $\vec{P}$. In contrast, little is known about the essential mechanism of multiferroics in TbMn_2O_5 due to its structural complexity. The exact relation and interplay between AFM ordering and ferroelectricity in frustrated magnetic systems are not known and remains controversial [50, 54, 60, 61, 62].

4.1.1 The Structure of TbMn$_2$O$_5$

Rare-earth manganese oxide $R\text{Mn}_2\text{O}_5$ (R = La,Y, rare earth, or Bi) have been studied for their unusual magnetic properties back to the 1960s. But very little is actually known about the ferroelectricity and magnetism of TbMn_2O_5, primarily owing to its chemical and structural complexity. This is related to the complexity of the TbMn_2O_5 crystal structure, where Mn^{4+}O_6 octahedra and Mn^{3+}O_5 pyramids
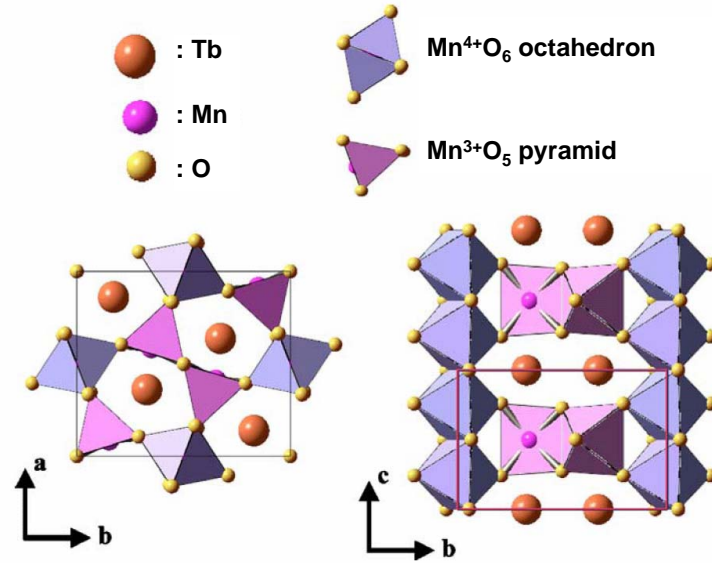
Figure 4.1: Crystal structure of TbMn$_2$O$_5$: View along the c axis (left panel) and along the a axis (right panel). From Higashiyama *et al.* [56]

are linked through edge- and corner-sharing networks, leading to five independent nearest-neighbor magnetic interactions. The crystal structure at room temperature is orthorhombic ($PBam$), as shown in Fig. 4.1. For dielectric constant measurement as shown in Fig. 4.2, the dielectric constant along the b axis shows anomalies. Upon cooling temperature, the dielectric constant starts to increase at $T \sim 43$ K. When temperature around 38 K, the spontaneous polarization along the b axis occurs and the dielectric constant shows a sharp peak with temperature. On further cooling, the dielectric constant shows a step-like increase at $T_{C2} \sim 23$ K.

Neutron diffraction studies have suggested a helical distribution of Mn moments rotating in the ab plane. Upon cooling below 42 K, the system enters a lock-in commensurate magnetic state with the magnetic propagation vector $q = (\frac{1}{2}, 0, \frac{1}{4})$ from a two-dimensionally modulated (2D) incommensurate magnetic one with the

temperature-dependent $q = (q_x, 0, q_z)$
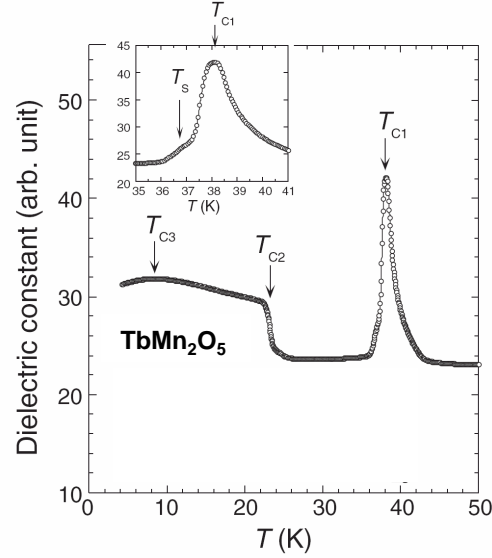
Figure 4.2: Dielectric constant along the b axis as a function of temperature. From Satoru Kobayashi *et al*.

4.2 Experimental Result

We measured Mn L_{III}-edge $(2p_{3/2} \rightarrow 3d)$ resonant soft-x-ray magnetic scattering on single crystals of $TbMn_2O_5$. Figure 4.3(A) illustrates a schematic view of our soft-x-ray scattering measurement. $TbMn_2O_5$ crystals were grown using $B_2O_3/PbO/PbF_2$ flux in a Pt crucible [50]. The flux was held at 1280 °C for 15 hours and slowly cooled down with a rate of 1 °C per hour to 950 °C. In the experiments, a $TbMn_2O_5(100)$ crystal with dimensions of $(2 \times 1 \times 1)$ mm^3 was cut and polished to achieve a mirror-like surface, followed by a high-temperature annealing. The momentum transfer $\vec{q}$ is in the scattering plane defined by the a and c axes, i.e., $\vec{q} = (q_x, 0, q_z)$. The instrumental
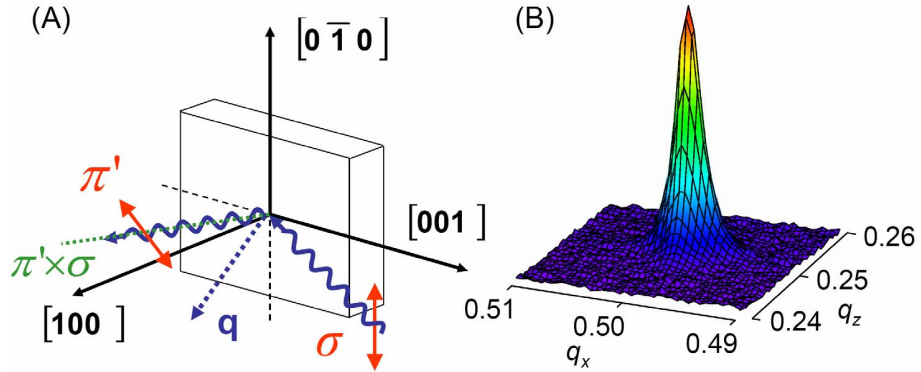
Figure 4.3: (A) Schematic view of resonant soft-x-ray magnetic scattering measurements on TbMn$_2$O$_5$(100) with σ and π' polarizations for incident and scattered photons, respectively; (B) Intensity of resonant scattering plotted in the $q_x q_z$ plane at 30 K with photon energy of 639 eV.

resolution in both q_x and q_z is estimated to be $\simeq 0.0005 \mathring{A}^{-1}$ at the Mn L-edge. The

electric vector e of incident soft x-rays is switchable to be parallel (σ polarization)

or perpendicular (π polarization) to the b axis. To minimize self absorption, we

used photons with an energy just below the Mn L_3-edge absorption; for example, the

penetration depth ($\sim 1800 \mathring{A}$) of 639-eV photons is much larger than the correlation

length ξ of AFM ordering, as shown below. Figure 4.3(B) is a plot of intensity

of resonant scattering with $\vec{q}$ around (1/2, 0, 1/4) in the reciprocal lattice units

measured at a sample temperature of 30 K using 639 eV photons of σ polarization.

A pronounced scattering intensity at the momentum transfer (1/2, 0, 1/4) clearly

demonstrates that TbMn$_2$O$_5$ exhibits an AFM ordering with a modulation vector

commensurate with the lattice, as observed in neutron measurements [53, 54]. The

curves of scattering intensity versus q along the a and c axes, i.e., q_x and q_z scans, were

fitted with a Lorentzian function and a linear background to obtain the scattering

intensity and the full widths at half maxima (FWHM).
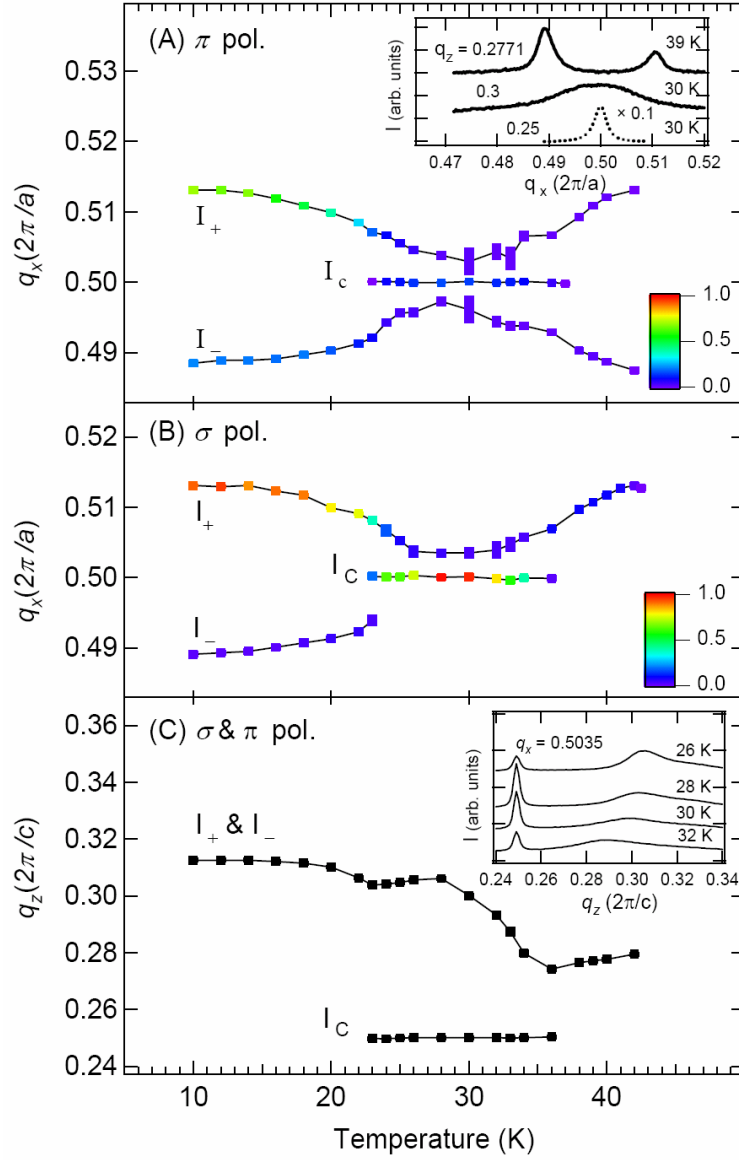
Figure 4.4: Temperature-dependent q of AFM ordering of TbMn$_2$O$_5$: (A) and (B) q_x component measured with π and σ polarizations; (C) q_z component. The vertical size of rectangular symbols indicates the uncertainty of q_x and q_z measurements. The insets of (A) and (C) are, respectively, scattering intensities I of q_x and q_z scans at selected temperatures.

To explore the coupling between FE and AFM, we measured temperature-dependent AFM ordering in $TbMn_2O_5$. The AFM ordering occurs with modulation vectors

$$((1/2) \pm \delta_x, 0, (1/4) + \delta_z) \tag{4.1}$$

in which δ_x and δ_z characterize the incommensurability of AFM ordering. The temperature dependence of q_x is plotted in Fig. 4.4(A) and (B) for π and σ polarizations, respectively. Intensities normalized to the scattering intensity of the commensurate AFM ordering at 30 K with σ polarization are expressed by means of color. The temperature dependence of q_z is plotted in Fig. 4.4(C) without showing relative intensities. We denote the scattering intensities of IC AFM ordering with $\vec{q}=((1/2)\pm\delta_x, 0, (1/4) + \delta_z)$ as $I_\pm$, and of the commensurate ordering as I_C. In addition, I_σ and I_π are the average intensities for σ and π polarizations, respectively, i.e., $I_\pm \equiv (I_+ + I_-)/2$ for IC order and $I_{\sigma/\pi} \equiv I_C$ for commensurate order. Our measurements unravel that the IC AFM ordering of $TbMn_2O_5$ begins to develop at 42 K, in agreement with neutron results. When the temperature decreases from 42 K, the IC ordering appears with a correlation length ~ 400Å, as shown in Fig. 4.5(A). For a temperature below 37 K, the IC scattering intensity decreases monotonically; the correlation length starts to decrease and becomes ~ 100 Åat 32 K. In addition, the q_x of the IC ordering moves toward 0.5 and then starts to depart from 0.5 about 30 K. In contrast, the commensurate ordering I_C appears between 37 K and 24 K with a correlation length ~ 500Å, coexisting with the IC ordering. The scattering intensities plotted in the insets of Fig. 4.4(A) and Fig. 4.4(C) demonstrate the coexistence of commensurate and IC AFM orderings. On the other hand, as shown

in Fig. 4.5(B), the onset of spontaneous electric polarization is accompanied by the incommensurate-commensurate AFM transition at 37 K, contrary to $TbMnO_3$ (11). On further lowering the temperature, a commensurate-incommensurate transition occurs at 23 K; the commensurate ordering disappears and the correlation length of IC ordering increases to ~ 400 Å. At this temperature, the electric polarization decreases and the dielectric constant ε shows a step-like structure.

The polarization dependence of the measurement provides information about the direction of magnetic moments. Hannon *et al*. proved that the scattering amplitude from resonant x-ray scattering contains a polarization factor $(e'^* \times e) \cdot \hat{Z}$, in which $e'^* \times e$ determines the direction of the magnetic moments $\hat{Z}$ probed with resonant scattering. Here e' is the electric field of the scattered light. With $\vec{q}$ near (1/2, 0, 1/4), the angle between the scattered x-ray and the a axis is $\sim 6°$ and that between the incident x-ray and the c axis is $\sim 19°$, as illustrated in Fig. 1(a). For an incident x-ray of σ polarization, the scattered x-ray with $e' \| b$ (denoted as σ' polarization) makes no contribution to the magnetic scattering, and the scattered x-ray with $e' \perp b$ (π' polarization) is predominantly sensitive to the magnetic moment along the a axis, i.e., $|S_q^a|$, because $\pi'^* \times \sigma$ is $\sim 6°$ away from the a axis. Conversely, if the incident x-ray has π polarization, the scattered x-ray has either π' or σ' polarization; $\pi'^* \times \pi$ is parallel to the b axis, whereas $\sigma'^* \times \pi$ is predominantly along the c direction. As neutron measurements indicate that the magnetic moments of $TbMn_2O_5$ are in the ab plane, the resonant scattering with π polarization is predominantly sensitive to the magnetic moment along the b axis, i.e., $|S_q^b|$. Hence the ratio of I_σ to I_π is

proportional to $|S_q^a|^2/|S_q^b|^2$. The knowledge of $|S_q^a|/|S_q^b|$ enables one to investigate how the spontaneous electric polarization $\vec{P}$ is induced by magnetization.

Combining the symmetry consideration, we can fellow the electric polarization well [67]. Figure 4.5(B) shows the comparison of P with the sum of the intensities $(I_\sigma I_\pi)^{1/2}$ over commensurate and incommensurate magnetic orderings.
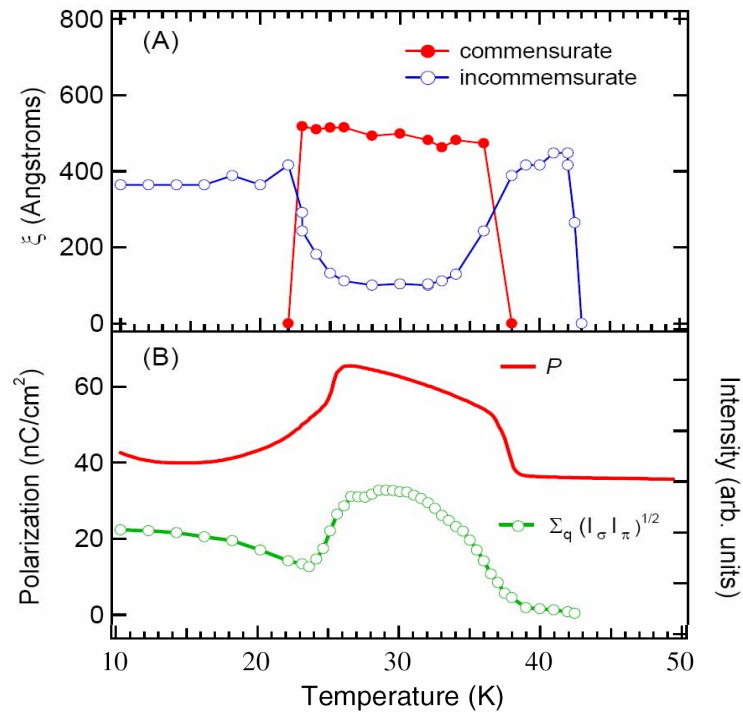
Figure 4.5: Temperature dependence of AF ordering and ferroelectric properties of TbMn$_2$O$_5$: (A) Correlation length ξ defined as 1/FWHM from the q_x scan; (B) Comparison of the spontaneous electric polarization P and intensities $\sum_q(I_\sigma I_\pi)^{1/2}$.

To conclude, our measurements of resonant soft-x-ray magnetic scattering reveal the intricate interplay between antiferromagnetism and ferroelectricity in TbMn$_2$O$_5$. Commensurate and IC AFM coexist at temperatures between 23 K and 37 K, in

contrast to earlier neutron results. Furthermore, the vector product of magnetization determines the spontaneous electric polarization. These facts provide a coherent picture of multiferroic behaviors in $TbMn_2O_5$ and also provide a fundamental symmetry constraint on the microscopic mechanism of multiferroics.

Chapter 5

Charge, Orbital, and Spin Order in Layered Manganite

5.1 Effect of One-electron Bandwidth and Quenched Disorder

Manganites are interest for their electronic and many other properties, such as meatal-insulator transition and colossal magnetoresistance. One-electron bandwidth and the variance of ionic radius (quenched disorder) in the ABO_3 material, as shown in Fig. 5.1, are keyfactors for the existence of the charge-orbital ordering tendency [68, 69]. The A-site ionic radius decreases with an increase of the transition temperature of charge-orbital order ($T_{\mathrm{CO-OO}}$). The temperature of metal-insulator transition exhibits an almost linearly inverse relation with the tolerance factor, Γ, where $\Gamma = (r_\mathrm{A} + r_\mathrm{O})/\sqrt{2}(r_\mathrm{B} + r_\mathrm{O})$ in crystal with ABO_3 compound. The r_B and r_O indicate the ionic radii of transition metal and oxygen atoms, respectively. The composition of A-site atoms composed of by alkali earth ions (divalent) and rare earth ions (trivalent), $r_A = (1-x)r_{\mathrm{RE}}^{3+} + xr_{\mathrm{AE}}^{2+}$, affects the population of the B-site valence electrons. For
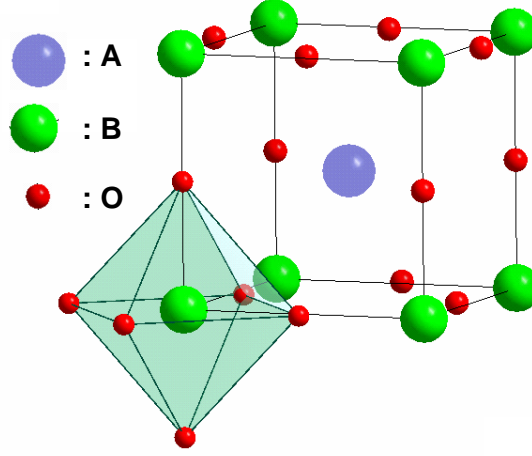
Figure 5.1: Illustration of ABO_3 structure.

$\Gamma = 1$, the crystal structure is undistorted; the B-O-B bonds is straight and the bond angle (θ) between t_{2g} states at two B-site atoms equal to 180°. By decreasing the A-site ionic radius, the oxygen atoms tend to move to the center of unit cell and the bond angle gets smaller than 180°. The probability of electron hopping amplitude between two nearest-neighbor Mn atoms decrease by $\cos\frac{\theta}{2}$ as the bond angle decreases [73]. At the same time, the decrease in the overlap between B-site atoms and oxygen narrows the bandwidth between two nearest-neighbor B-site atoms. Finally, when the energy band gap appears, the system is insulating which is related to charge-orbital order. Therefore, as a reduction of A-site ionic radius and tolerance factor, the temperature of metal-insulator transition increases. In addition to the one-electron bandwidth, the parameter of ionic radius variance σ^2 can also affect the T_{CO-OO}. The quenched disorder which associated with the chemical composition of the A-site ions can be quantified by using the ionic radius variance defined as $\sigma^2 = \sum_i x_i r_i^2 - r_A^2$. The x_i and r_i are the fractional occupancies ($\sum_i x_i = 1$) and electronic radii of the different
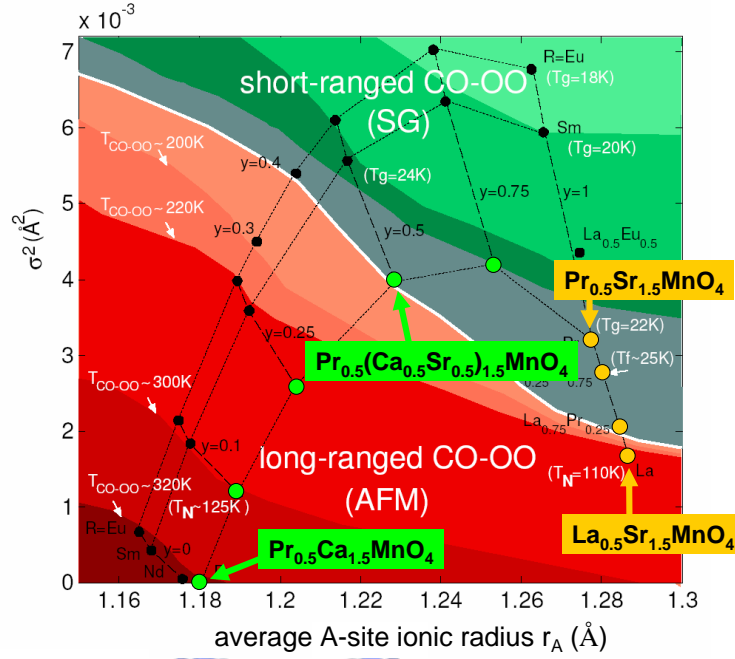
Figure 5.2: Electronic phase diagram of $R_{0.5}(Ca_{1-y}Sr_y)_{1.5}MnO_4$ in the plane of the average ionic radius r_A and the variance σ^2 from Mathieu et $al.$[70].

i cations on the A-site, respectively, and $r_A = \sum_i x_i r_i$. The T_{CO-OO} decreases with the increase of variation [69].

5.1.1 Charge, Orbital, and Antiferromagnetic order of $La_{0.5}Sr_{1.5}MnO_4$ and $Pr_{0.5}Ca_{1.5}MnO_4$

Below the Neel temperature (T_N), charge-orbital and magnetic order coexist in the MnO_2 plane of sing-layered half-doped compound in $La_{0.5}Sr_{1.5}MnO_4$ (LSMO) and $Pr_{0.5}Ca_{1.5}MnO_4$ (PCMO). A phase diagram for $R_{0.5}(Ca_{1-y}Sr_y)_{1.5}MnO_4$ versus A-site ionic radius and variation is shown in Fig. 5.2 [70]. LSMO has a larger $r_A (\sim 1.28 \mathring{A})$ than that of PCMO ($\sim 1.18 \mathring{A}$). In addition, PCMO has a much smaller

Figure 5.3: Picture of LSMO sample.

quenched disorder ($\sigma^2 \sim 2 \times 10^{-7} \mathring{A}$ for PCMO and $\sigma^2 \sim 10^{-3} \mathring{A}$ for LSMO). The temperatures of charge-orbital order transitions are 235 K and 320 K for LSMO and PCMO, respectively. In addition, the antiferromagnetic (AFM) orders exist below 110 K and 125 K, the Neel temperature, for LSMO and PCMO, respectively. For these two compounds, the differences are A-site ionic radius, quenched disorder and electronic structure between PCMO and LSMO.

High-quality single crystals of LSMO and PCMO were grown by Mathieu *et al.* using floating zone method [70]. Figure 5.3 is the picture of our LSMO sample. The structure with the crystal space group $I4/mm$, and $a = b = 3.86(3.82)\mathring{A}, c = 12.44(12.66)\mathring{A}$ for LSMO (PCMO) is shown in Fig. 5.4 (A). As illustrated in Fig. 5.4 (B), Mn ions in LSMO and PCMO order in an alternating Mn^{3+}/Mn^{4+} pattern in the MnO_2 plane below the charge-orbital transition temperature. Red and green symbols denote the e_g orbitals on the Mn^{3+} sites. Below T_{CO}, the charge-orbital order with the modulation vector $\vec{q} = (1/4, 1/4, 0)$ takes place and the unit cell shows with the brown rectangle [71, 72, 93]. Below T_N, there also exist ferromagnetic zigzag chains of Mn^{3+} and Mn^{4+} bridged by oxygens with Mn^{4+} situated on the corner sites [12]. The
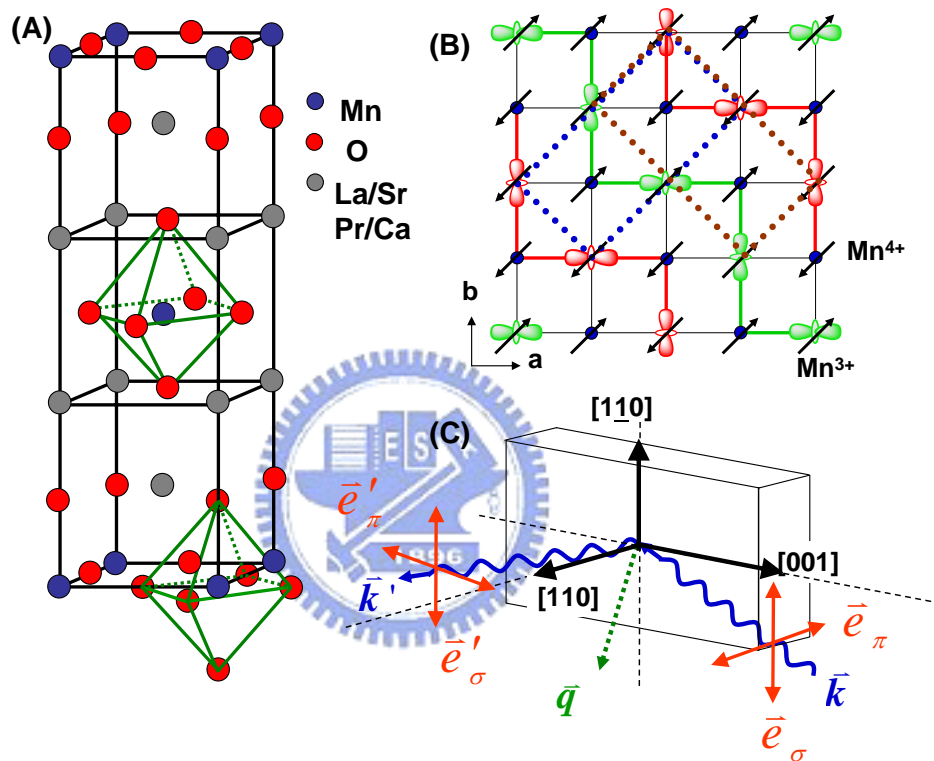
Figure 5.4: A) Illustration of the structure of the half-doped single-layered manganite.(B) Illustration of the spin-charge-orbital order in the MnO_2 plane. Red and green symbols denote the e_g orbitals on the Mn^{3+} sites. Solid green and red lines indicate ferromagnetic zigzag chains with opposite magnetic moments. Oxygen atoms are omitted for clarity. The in-plane unit cells of the charge-orbital order (brown) and AFM order (blue) are indicated with dotted rectangles; (C) Schematic view of the soft-x-ray scattering geometry with $\vec{k}$ and $\vec{k}'$ denoting the wave vectors of incident and scattered photons, respectively. The [110], $\vec{q}$, and horizontal polarization vector e_σ are in the scattering plane.

spins between zigzag chains are AFM coupled via the superexcahnge interactions. Solid green and red lines indicate ferromagnetic zigzag chains with opposite magnetic moments. The blue rectangles indicate the AFM order with the same modulation vector $\vec{q} = (1/4, 1/4, 0)$ of charge-orbital order by rotated 90 degree. In addition, the MnO_2 planes stack one over another by a displacement of the lattice constant c along the z direction, with identical Mn charges and orbitals but reversed spins. The non-zero interlayer exchange coupling leads to a 3D AFM order with a modulation vector of $(1/4, 1/4, 1/2)$.

5.1.2 Experimental Result

Crystals of LSMO and PCMO cut with a (110) surface were aligned in a two-circle diffractometer with [110] in the scattering plane. The [001], $\vec{q}$, and horizontal polarization vector e_π are also in the scattering plane. The photon energy was tuned about the L-edge $(2p_{3/2} \rightarrow 3d)$ absorption of Mn and the energy resolution was 0.14 eV at 640 eV. For σ polarization, the $\vec{e}$ vector of incident light was perpendicular to the scattering plane.

Charge-orbital and magnetic orders show anisotropy with its local $\hat{\mathbf{z}}$ direction. In an electric-dipole transition, the scattering amplitude f^{E1} is proportional to $(\mathbf{e}_s^* \cdot \hat{\mathbf{z}})(\mathbf{e}_i^* \cdot \hat{\mathbf{z}})([2F_{1,0} - F_{1,1} - F_{1,-1}]) + (\mathbf{e}_s^* \times \mathbf{e}_i) \cdot \hat{\mathbf{z}}_m[F_{1,1} - F_{1,-1}]$ [18]

As temperature cooling down, AFM phases exist in LSMO and PCMO under T_N. The curve (A) and (B) in Fig. 5.5 are the measured energy-dependent spectra with the scattering vector $\vec{q} = (1/4, 1/4, 1/2)$ AFM order in LSMO and PCMO,
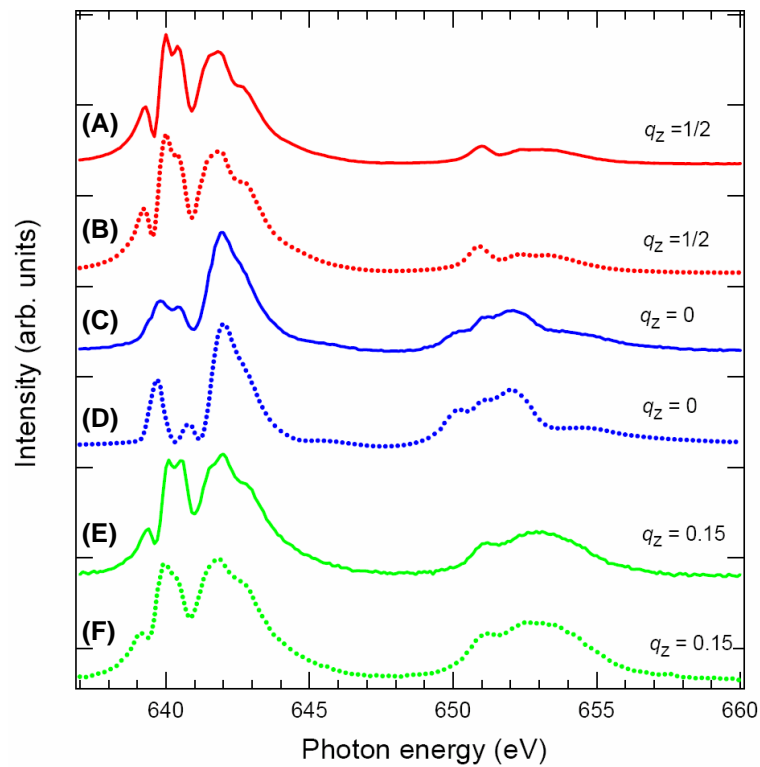
Figure 5.5: Photon-energy dependence of the resonant soft-x-ray scattering of charge-orbital and AFM order in LSMO (solid line) and PCMO (dotted line). Spectrum (A) is the AFM order in LSMO with $T = 100$ K. Spectrum (B) is the AFM order in PCMO with $T = 80$ K. Spectrum (C) is the charge-orbital order in LSMO with $T = 100$ K. Spectrum (D) is the charge-orbital order in PCMO with $T = 80$ K. Spectrum (E) is the 2D AFM order in LSMO with $T = 90$ K. Spectrum (F) is the 2D AFM order in PCMO with $T = 114$ K. All spectra are normalized to have the same intensity at 642 eV and vertically offset for clarity.

respectively. The line shape of the energy scan of spectrum (A) has been established experimentally and theoretically [84]. We found the line shapes of 3D AFM order in LSMO and PCMO are nearly identical, even thought the difference of the ionic size. The AFM orders in LSMO and PCMO exhibit the same character. By the energy scan of 3D AFM order, we can not conclude the one-electron bandwidth or quenched disorder affect T_N. Because the modulation vectors are the same, the scattering intensity originated from AFM order stacking along c-axis with difference spin. However for orbital order, the line shape around L_3 is different between LSMO and PCMO. The curve (C) and (D) are the energy-dependent spectra with $\vec{q} = (1/4, 1/4, 0)$ charge-orbital order in LSMO and PCMO. We found that around the line shape around L_3 is quite different, while the difference in the line shape around L_2 is small. The scattering intensity is vary sensitive for the electronic structure of $3d$ band of Mn ion. By changing the A-site ionic radius and the variation, the energy level of each orbital might change. We will seek for theoretical interpretation of these spectra.

In addition to the 3D AFM order, the 2D AFM and charge-orbital order orders coexist in LSMO and PCMO below T_N. Figure 5.6(C) is the contoured plot of scattering intensity of LSMO in the plane defined by q_{110} and q_{001}. The strongest intensity is of $(1/4, 1/4, 1/2)$ 3D AFM order. The other peak is of $(1/4, 1/4, 0)$ charge-orbital order. Between these two peaks, there is a feature along the q_{001} direction in LSMO. Figure 5.6 (A) are the q_Z scans fixed at $q_{110} = 0.25$ of Mn L-edge resonant scattering
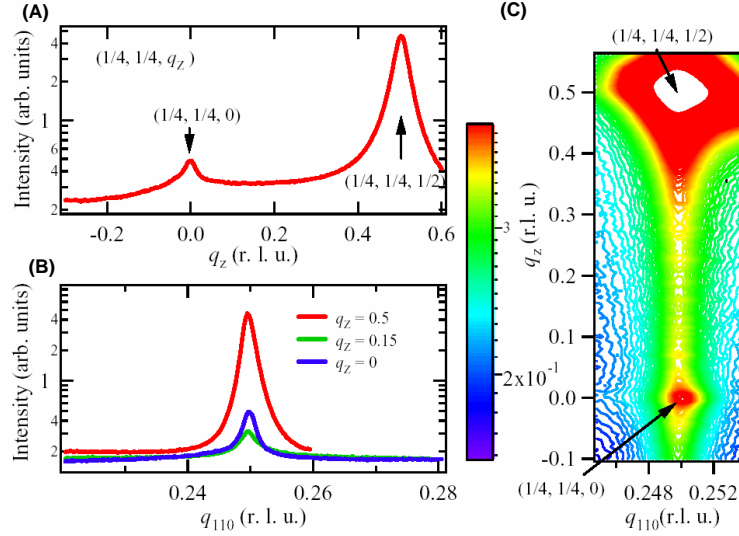
Figure 5.6: (A) and (B): Momentum scans of Mn L-edge resonant scattering from LSMO with scan of momentum transfer q along the [001] and [110] directions. (C)Intensity contour of Mn L-edge resonant scattering from LSMO plotted in the plane defined by q_{110} and q_z at 100 K with photon energy of 639 eV.

from LSMO, and Fig. 5.6 (B) are the q_{110} scans fixed at $q_Z = 0.5$, 0.15, 0, respectively. The q_{110} and q_Z scans with $q = (1/4, 1/4, 0.15)$, indeed, show anisotropic in q dependence (like a stripe). This stripe supports that the in-plane order exists in LSMO. In order to get the origin of these in-plane order, we do the energy scan with selected $q_z = 0.15$, as shown in Fig. 5.5 (E). We found the energy spectrum of this in-plane order is nearly identical to that of 3D AFM order, but dramatically different from that of charge-orbital order. Therefore, we conclude that this in-plane order is of AFM order. In addition to LSMO, PCMO also exhibits the 2D AFM order below T_N. In Fig. 5.5 (F), it shows that the origin of this in-plane order comes from magnetic order in PCMO. For 2D AFM order in LSMO, not only exists blow T_N, but also above T_N. Actually, we found the 2D to 3D AFM order transition at T_N. This

issue will be discussed in next section.

One interest question is that if the La and Sr are replaced by Pr and Ca, the bond angle of Mn-O-Mn bends in the MnO plane, and T_N of 3D AFM order increases. Figure 5.7 (A) depicts the temperature dependence of the scattering intensity in PCMO and LSMO with $\vec{q} = (1/4,\ 1/4,\ 1/2)$ 3D AFM order. As the temperature increases, the scattering intensity decreases abruptly and reduces to nearly zero at temperatures about 113 K and 124 K, T_N of the 3D AFM order, for LSMO and PCMO,respectively. The Neel temperature of 3D AFM order in PCMO is higher by 11 K than that in LSMO.

We also measured the correlation lengths along the [1 1 0] and the [0 0 1] directions, denoted as ξ_{110} and ξ_{001}, respectively. LSMO and PCMO with momentum transfer q along these two directions, i.e., q_{110} and q_{001}. The correlation length is defined as the inverse of the half-width at the half-maxima in the q scan. Figure 5.8 shows the momentum-transfer dependence of (1/4, 1/4, 1/2) 3D AFM order at $T = 100$ K in PCMO and LSMO. The measured ξ_{110} and ξ_{001} are 408 and 80 Å, respectively, for LSMO, and 298 and 121 Åfor PCMO. The in-plane correlation ξ_{110} of LSMO is larger than that of PCMO; but the out-of plane correlation ξ_{001} of LSMO is smaller than that of PCMO. In addition, comparing the ratio of ξ_{001}/ξ_{110}, we found that the ratio in the AFM order of PCMO is 0.41, significantly larger than that of LSMO, 0.2. PCMO exhibits a more 3D-like AFM order than that of LSMO. The correlation lengths measured in the two compounds with AFM order, we show that the reduction in one-electron bandwidth and quenched disorder enhances the stabilization of 3D
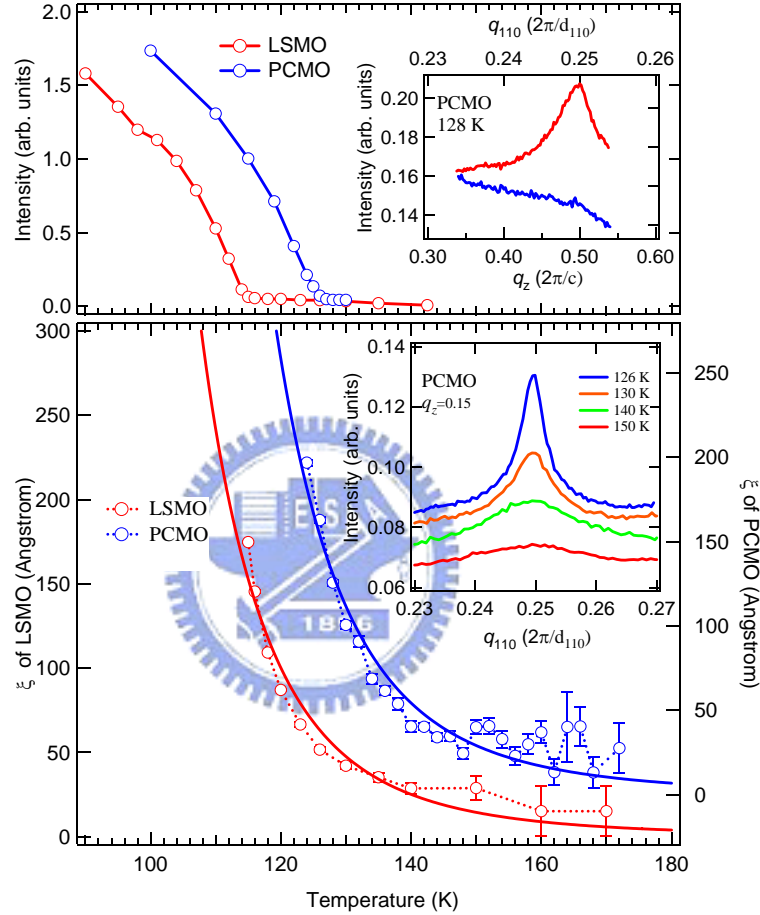
Figure 5.7: Temperature-dependent soft-x-ray scattering of LSMO (red line) and PCMO (blue line) with $h\nu = 640$ eV. (A) Scattering intensity from $\vec{q} = (1/4, 1/4, 1/2)$ of 3D AFM order; (B) In-plane correlation lengths ξ_{110} form $\vec{q} = (1/4, 1/4, 0.15)$ with solid curves of $e^{2\pi JS^2/kT}$ using $J = 7.1 \pm 0.6$ and 8 ± 0.6 meV for LSMO and PCMO, respectively. Inset: (A) q_{110} and q_{001} scans of $(1/4, 1/4, 1/2)$ at 128 K with vertical offsets for clarity. (B) q_{110} scans of $\vec{q} = (1/4, 1/4, 0.15)$ at selected temperatures with vertical offsets.
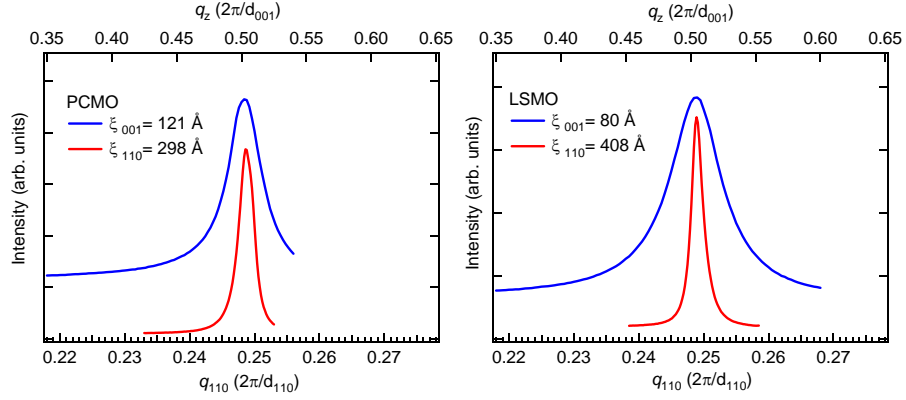
Figure 5.8: Momentum-transfer dependence of Mn L-edge resonant $(1/4, 1/4, 1/2)$ scattering of LSMO and PCMO along the $[1\,1\,0]$ and $[0\,0\,1]$ directions recorded at 100 K with $h\nu = 640$ eV.

AFM order.

For 2D AFM order, in addition to LSMO, PCMO sample also exhibits the 2D AFM order above T_N, as shown in the inset of Fig. 5.7(A). These are the q_{110} scan fixed at $q_z = 0.5$ and q_z scan fixed at $q_{110} = 0.25$ on PCMO above T_N. In q_{110} scan, there is a well-defined peak, but in q_{001} the line shape is quite flat. This also suggests that the 2D-to-3D AFM ordering transition exists at T_N in PCMO.

We further checked the one-electron bandwidth and quenched disorder effects for 2D AFM order in both layered compound. The inset of Fig. 5.7 (B) is the q_{110} scans of $\vec{q} = (1/4, 1/4, 0.15)$ of PCMO at selected temperatures with vertical offsets. The line shape still exists above T_N. It also exhibits 2D AFM order above T_N in PCMO. To further understand the behavior of the spin-spin correlation of the 2D AFM order in CE type single-layered manganites, we analyzed the temperature dependence of ξ. Figure 5.7 (B) is the correlation length ξ_{110} in PCMO and LSMO above T_N. We fitted the temperature dependence with $\xi \sim e^{2\pi\rho_s/kT}$, where k is the Boltzmann constant,
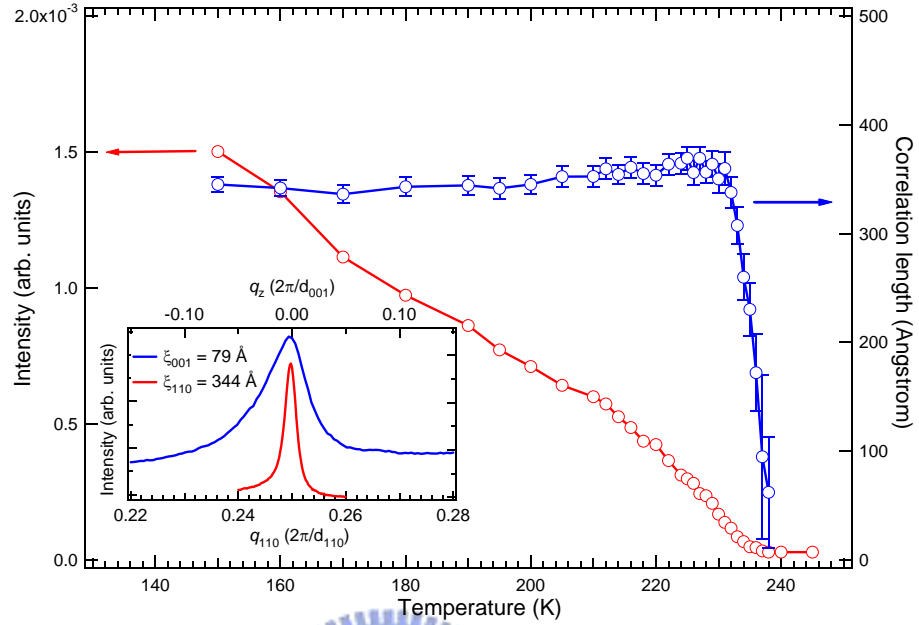
Figure 5.9: Temperature-dependent soft-x-ray scattering of LSMO along [110] with $h\nu = 642$ eV and $\vec{q} = (1/4, 1/4, 0)$. Red and blue lines are the Scattering intensity and correlation length from charge-orbital order. Inset: Momentum-transfer dependence of Mn L-edge resonant (1/4, 1/4, 0) scattering of LSMO along the [1 1 0] and [0 0 1] directions recorded at 100 K.

and ρ_s is the spin stiffness; the relation between ρ_s, spin S, and in-plane Heisenberg exchange coupling J is $\rho_s = JS^2$. Assume that $S^2 = 3$ for half-doped mixed valence manganites, we found that the in-plane exchange coupling constant of LSMO and PCMO are close, i.e., $J = 5.5 \pm 0.5$ meV for LSMO and $J = 6.0 \pm 0.5$ meV for PCMO. The J values between PCMO and LSMO show no dramatically difference. Therefore, the analysis of spin-spin correlation, we failed to find the relation between 2D AFM order and A-site ionic radius and quenched disorder.

Figure 5.9 is the temperature-dependent of soft-x-ray scattering of LSMO. The intensity of (1/4, 1/4, 0) charge-orbital order decreases with the increase of temperature. The $T_{\text{CO--OO}}$ is 238 K. For the correlation length of (1/4, 1/4, 0) charge-orbital
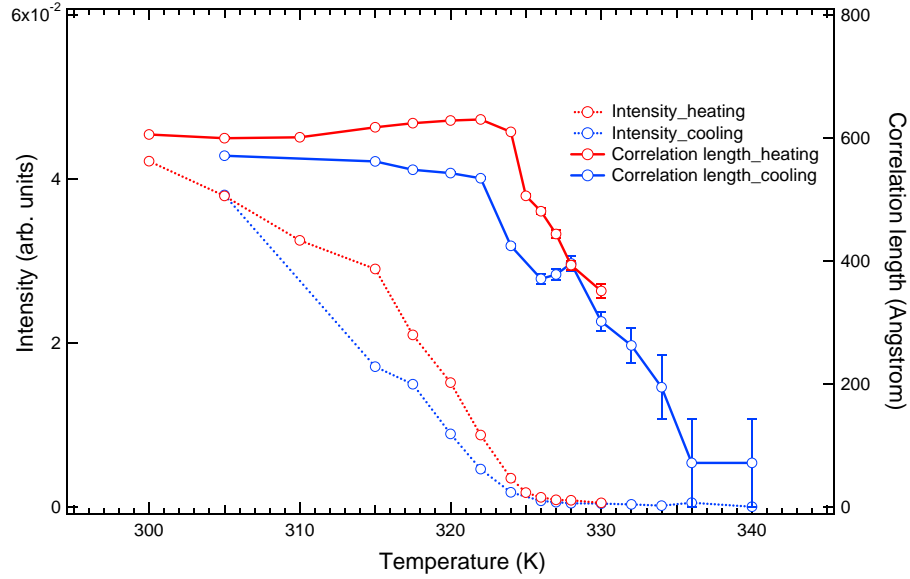
Figure 5.10: Temperature dependence of $\vec{q}$ around $(1/4, 1/4, 0)$ soft-x-ray scattering of PCMO with $h\nu = 640$ eV along [001] direction. Red and blue lines are the Scattering intensity and correlation length from charge-orbital order.

order, it does not decrease with increasing temperature below the T_{CO-OO}; and it decreases rapidly above 231 K. The inset of Fig. 5.9 indicate the correlation length of charge-orbital order is anisotropic in LSMO.

Figure 5.10 is the temperature-dependent of $(1/4, 1/4, 0)$ charge-orbital order of PCMO. The intensity of $(1/4, 1/4, 0)$ charge-orbital order nearly disappear at T_{CO-OO} = 325 K. As the temperature increases and approaches T_{CO-OO}, the correlation length of $(1/4, 1/4, 0)$ charge-orbital order tends to increase and then start to decrease rapidly when the temperature is above 325 K. Unlike 2D AFM order, They do not exhibit 2D charge-orbital order in PCMO and LSMO for temperature above the T_{CO-OO}.

Noticeable, the charge-orbital order of PCMO shows the self-absorbtion effect.
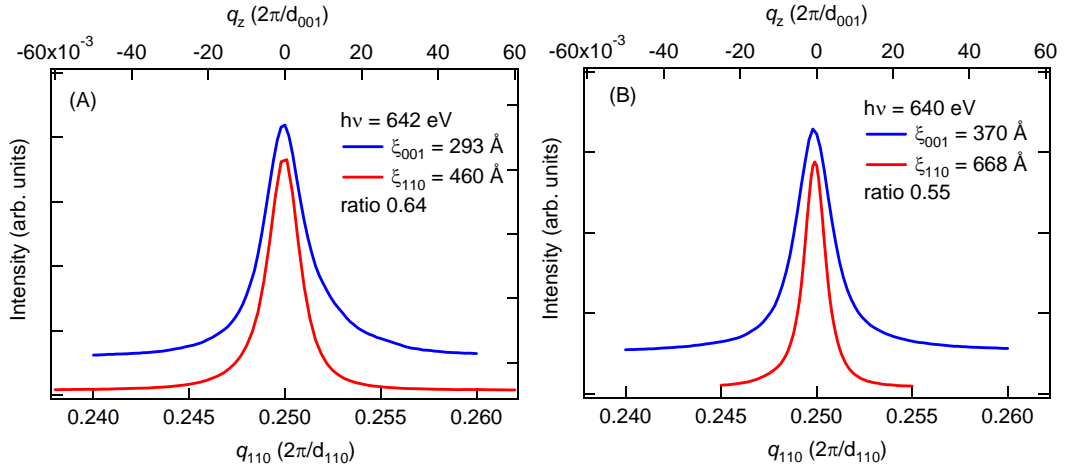
Figure 5.11: Momentum-transfer dependence (1/4, 1/4, 0) scattering of PCMO along the [1 1 0] (red line) and [0 0 1](blue line) directions recorded at 100 K under different photon energy (A) $h\nu = 642$ eV ; (B) $h\nu = 640$ eV.

Figure 5.11 is the momentum-transfer dependence charge-orbital ordering along the [1 1 0] and [0 0 1] direction with difference photon energy. The correlation length probing with $h\nu = 640$ eV is larger than that with $h\nu = 642$ eV. The measured ξ_{110} and ξ_{001} are 668 and 370 Å, respectively. It decreases to 460 and 293 Åby changing the photon energy from $h\nu = 640$ eV to 642 eV. The ratio of ξ_{001} / ξ_{110} also changes from 0.55 to 0.64.

Like 3D AFM order, PCMO exhibits more 3D character of charge-orbital order than LSMO. Although the deviation of ratio exists by changing the photon energy. The ratio ξ_{001}/ξ_{110} of charge-orbital in PCMO is much larger than that in LSMO with the same measured photon energy. The inset of Fig. 5.9 display (1/4, 1/4, 0) charge-orbital orders in LSMO along [110] and [001] directions with $T = 100$ K. The measured ξ_{110} and ξ_{001} are 340 and 75 Å, respectively, for LSMO. The ratio of ξ_{001}/ξ_{110} in the orbital ordering of LSMO is 0.22. The ratio of PCMO is significantly larger

than that of LSMO. Compared with correlation lengths of charge-orbital order in LSMO and PCMO, PCMO exhibits more 3D character in charge-orbital order. The transition temperature of charge-orbital order in PCMO is much higher around 100 K than in LSMO. Therefore, we show that the reduction in one-electron bandwidth and quenched disorder strongly enhances the stabilization of charge-orbital ordering.

We also considered about the correlation length of AFM and charge-orbital ordering in both LSMO and PCMO. As above mention, the ξ_{110} of AFM order in LSMO (408 Å) is larger than that in PCMO (298 Å). But for charge-orbital order, the ξ_{110} of charge-orbital order in LSMO (344 Å) is smaller than that in PCMO (460 Å). For ratio of AFM and charge-orbital order seems no changed in LSMO. For PCMO the ratio of charge-orbital order enhanced comparing with the ratio of AFM order. But the scattering intensity of the (110) of LSMO is much stronger indicating the crystal structure better than PCMO. For charge-orbital superstructure, the correlation length of PCMO is larger than that of LSMO. It strongly suggest the one-electron bandwidth and quenched disorder strongly affect the electron hopping integer which related to the charge-orbital order. The more stabilization of charge-orbital order is, i.e., large correlation length, the higher of transition temperature of charge-orbital order is. Therefore, based on the correlation lengths measured at the same temperature in the two compounds with different ordering temperatures, we show that the reduction in one-electron bandwidth and quenched disorder strongly enhances the stabilization of orbital ordering.

In conclusion, We present measurements of AFM and charge-orbital order on

single-layered manganites with different sizes of cations. Charge-orbital and 3D AFM order of PCMO exhibits a stronger 3D character and a dramatically enhanced transition temperature, as compared with those of LSMO. Our results indicate that reduction in one-electron bandwidth and quenched disorder strongly enhances the stabilization of charge-orbital order.

5.2 Quasi-Two-Dimensional Antiferromagnetism in LSMO

5.2.1 Low-Dimensional Quantum Magnetism

Magnetism in low dimensions has attracted much attention in the past two decades due to its relevancy to many important phenomena in condensed-matter physics [74]. At finite temperatures, as dictated by the Mermin-Wagner theorem [75], thermal fluctuations prevent long-range magnetic ordering for dimensions $d \leq 2$. The low-dimensional long-range magnetic order can thus survive only at zero temperature under the condition when quantum fluctuations are not too strong. For spin-$\frac{1}{2}$ quantum Heisenberg antifrromagnets (QHA) on two-dimensional (2D) square lattice, as clarified by the seminal work of Chkravarty *et al.* [76], the long-range AFM order dose survive out of quantum fluctuations in certain regime. In addition, the system exhibit renormalized classical behavior and the 2D zero-temperature AFM order extends out of finite temperatures with the spin correlation following exponential growth in inverse temperature. The illustration of 2D order with temperature has been shown in the Fig. 5.12. However, because real systems are three dimensional, the quasi-2D AFM order that extends to finite temperatures is masked by the 3D AFM transition at T_{N} and is exhibited only above T_{N} with a large 2D-like spin correlation length. In this case, the usually observed mean-field regime around T_{N} is replaced by the renormalized classical regime. This phenomenon has been confirmed in spin-$\frac{1}{2}$ cuprates [77, 78] with quantitative agreement, but its quantitative validity for other magnitudes of spins was later called into question [79]. Based on self-consistent quantum
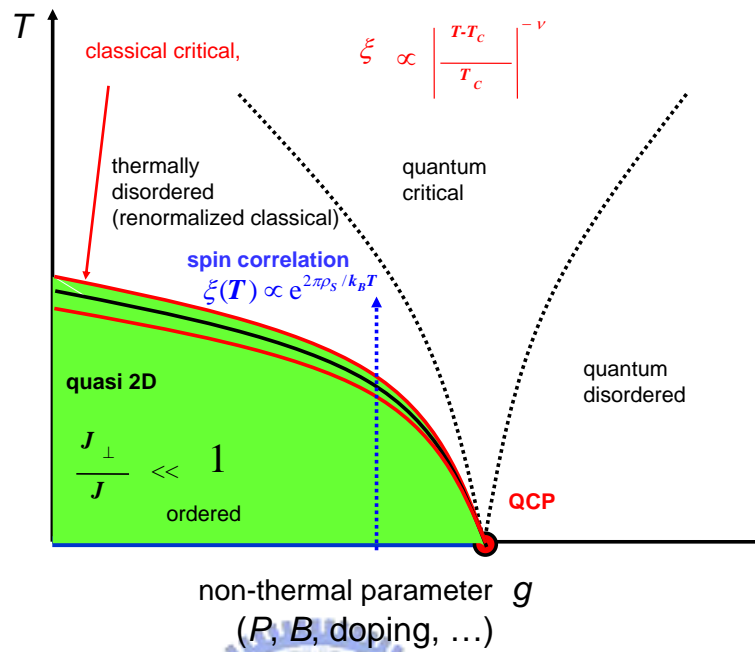
Figure 5.12: Illustration of 2D order with temperature

harmonic approximation, the theory is later refined so that quantitative validity for different spins can be reached [80, 81]. In real materials, however, magnetic interactions are usually much more complicated than those in QHA. Various types of AFM order exist in layered oxides [11, 12] and charge or orbital degrees of freedom may even be involved. For example, below Neel temperature, charge-orbital and AFM order coexist in half-doped single-layered LSMO. Figure 5.13(A) shows the structure of LSMO. Of particular importance is to examine if 2D-like AFM order survives above T_N in materials with strong coupling of spin, charge, and orbital degrees of freedom.

Figure 5.13: (A) Illustration of crystal structure in LSMO. (B) Illustration of charge-orbital and AFM order on MnO_2 plane. (C) In-plane AFM order unit cell in reciprocal space. (D) Antiferromagnetic coupling along c-axis.

5.2.2   Antiferromagnetic Transitions of LSMO

Similar to cuprates, LSMO also has distinct features of the MnO_2 plane in the perovskite structure. Nonetheless, instead of superconductivity, it exhibits charge-orbital order [19, 71, 92, 84, 82]. Furthermore, the antiferromagnetism 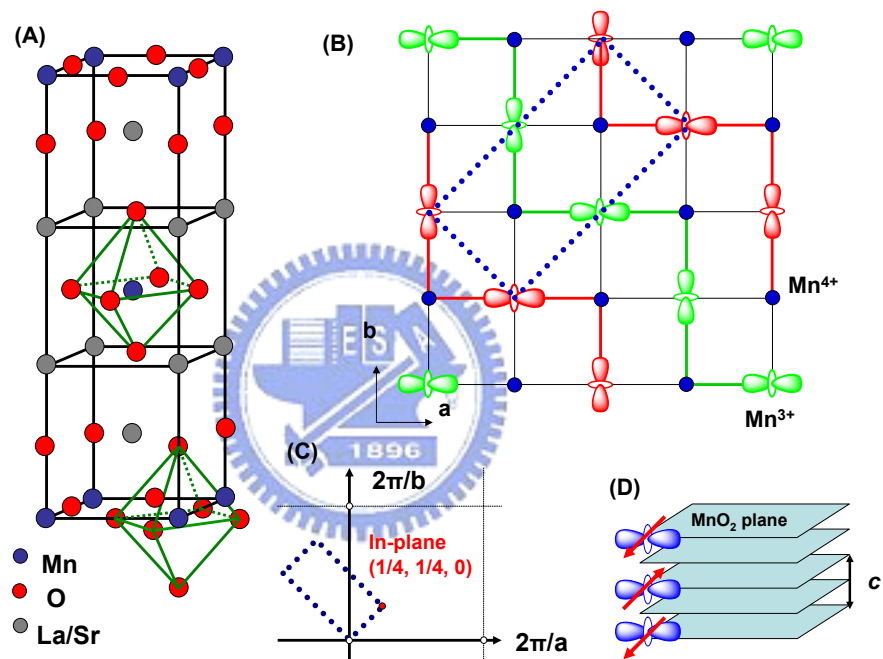in this system has 3D character with the so-called CE-type AFM structure [11, 12],which is essentially composed of ferromagnetic zigzag chains antiferromagnetically coupled to one-another. Sternlieb *et al.* [82] has proven the charge and spin order in MnO_2 plane. As illustrated in Fig. 5.13(B), Mn ions in LSMO order in an alternating Mn^{3+}/Mn^{4+} pattern in the MnO_2 plane below the charge-orbital transition temperature T_{CO-OO} = 220 K. Below T_N, there also exist ferromagnetic zigzag chains of Mn^{3+} and Mn^{4+} bridged by oxygens with Mn^{4+} situated on the corner sites. The spins between zigzag chains are AFM coupled via the superexcahnge interactions. A blue dotted rectangle in Fig. 5.13(B) indicates an in-plane unit cell of AFM order; the corresponding unit cell in the reciprocal space is also plotted in Fig. 5.13(C). Such an in-plane AFM order has a modulation vector (1/4, 1/4, 0) in the reciprocal lattice units. For example, Sternlieb *et.al.* showed the existence of (1/4, 1/4, 3/2) antiferromagnetic order measured by neutron diffraction. The Neel temperature is 110 K. The intensity decreases by increasing temperature, as shown in Fig. 5.14. In this study an ordering wave vector (1/4, 1/4, 1/2) has been observed with also a small intensity at $(h/4, h/4, 0)$ type positions as a minority stacking. In addition, along c-axis, the magnetic coupling is AFM couple, as illustrated in Fig. 5.13(D). The MnO_2 planes are stacked one over another by a displacement of the lattice constant c along the z direction,
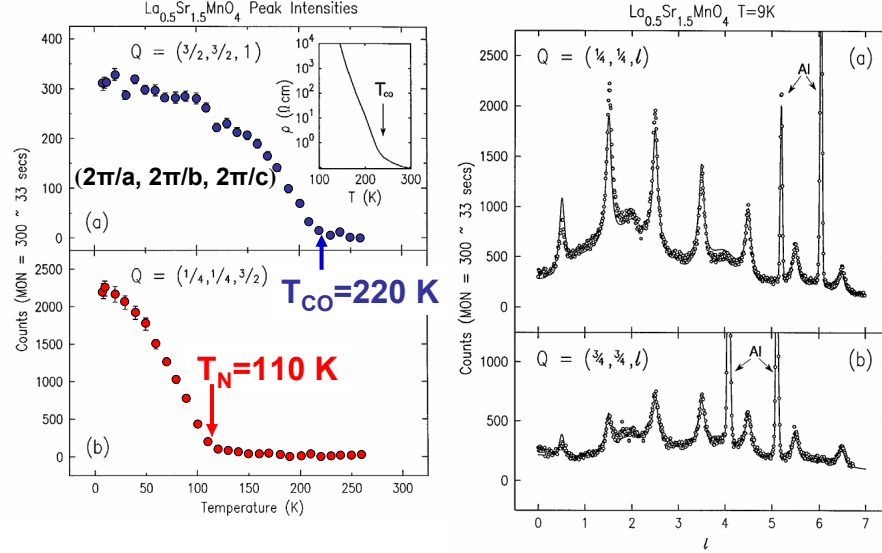
Figure 5.14: Neutron diffraction result of AFM order in LSMO from Sternlieb *et al.* [82]

with identical Mn charges and orbitals but reversed spins. The non-zero interlayer exchange coupling leads to a 3D AFM order with a modulation vector of (1/4, 1/4, 1/2). However, to date, there is no experimental work that clarifies the critical behavior of the corresponding AFM transition [82, 83, 84, 85, 86, 87, 88, 89, 90]. Only one information we can get is magnetic susceptibility measurement [71, 91, 95], as shown in Fig. 5.15. As we seen, the inset, there is an anomaly above Neel temperature. This anomaly seems to suggest that there is a 2D order transition. The important issue to be addressed is then if the system supports quasi-2D AFM order above T_N.

In this work, we investigate the quasi-2D AFM order in LSMO above T_N. Based on measurements of resonant soft-x-ray magnetic scattering, we unravel the nature of the AFM transition. Our results reveal that quasi-2D incommensurate AFM order exists at temperatures above T_N. The spin correlation length ξ is large, up to
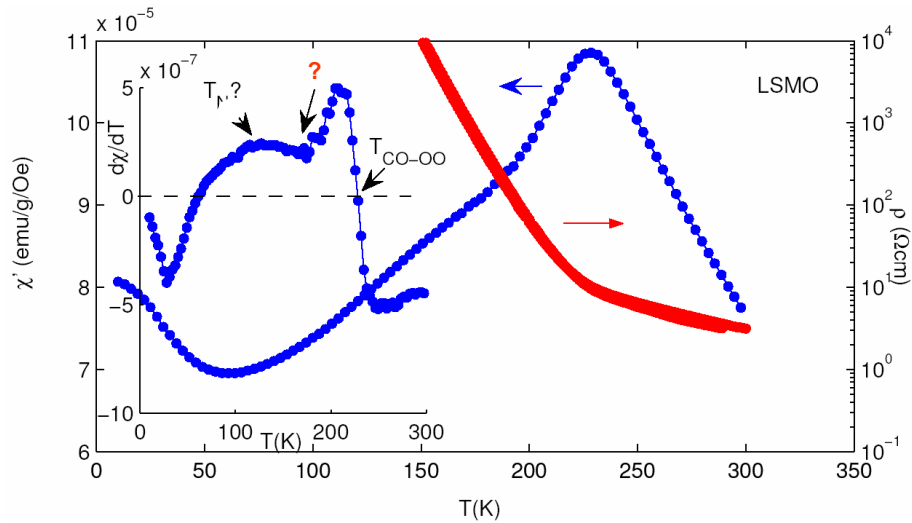
Figure 5.15: Susceptibility and resistivity measurement on LSMO from R. Mathieu *et al.* [95].

$\xi/a \sim 25$, where a is the in-plane lattice constant, and shows an exponential growth in inverse temperature, indicating the 2D semi-classical [80] nature of the AFM order. Remarkably, this material exhibits a lock-in transition from incommensurate to commensurate near T_N, which coincides with the dimensional crossover, lending further support for the 2D nature of AFM order above T_N.

5.2.3   Resonant Soft x-ray Scattering

Resonant x-ray scattering studies of LSMO were first attempted at the manganese K-edge. The Mn K-edge resonance, which involves virtual excitations from $1s$ to $4p$, is generally insensitive. More Recently, resonant soft x-ray scattering at the Mn L-edges has been used to direct observed the charge-orbital, and magnetic order in LSMO [93, 84, 85]. Figure 5.16 shows the experimental results cited from Wilkins *et al.* (left-hand graph) and Staub *et al.* (right-hand graph). The left-hand graph

is the energy scan of (1/4, -1/4, 1/2) magnetic order. The spectra are based on atomic multiplet calculation in a tetragonal crystal field with different e_g orbital, as shown in Fig. 5.16LH(a)(b). A good agreement was found between the experimental data and theoretical fits which included a realistic description of the spin direction. Staub *et al.* have performed resonant soft x-ray scattering experiments on LSMO, including for the first time azimuthal scans and polarization analysis, as shown in Fig. 5.16RH. They have been clarified that the (1/4, 1/4, 0) soft x-ray scattering originated not only from charge-orbital order but also from magnetic order below the Neel temperature.
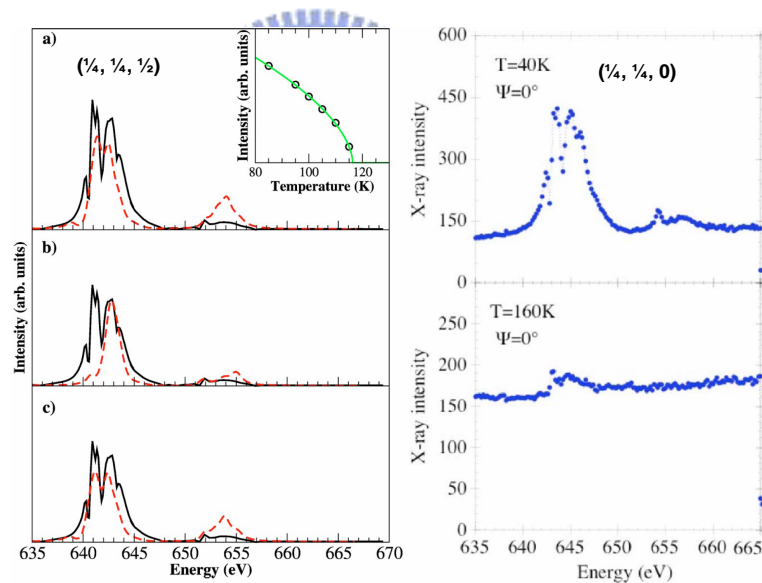
Figure 5.16: Left-hand graph from Wilkins *et al.* [84]: The energy scans of (1/4, -1/4, 1/2) resonant soft x-ray scattering. The inset shows the temperature dependence of magnetic order. Right hand graph from Staub *et al.* [86]: The energy scans of (1/4, 1/4, 0) resonant soft x-ray scattering.

Figure 5.17 illustrates a schematic view of scattering geometry. Single crystals of LSMO cut with a (110) surface were aligned in a two-circle diffractometer with [110]
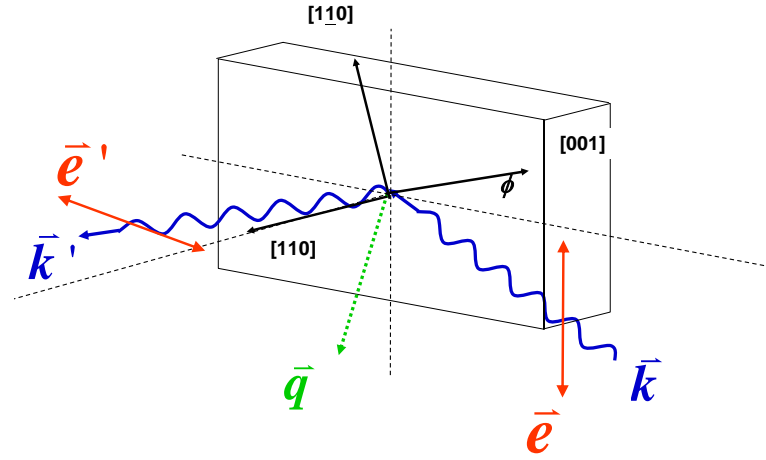
Figure 5.17: Schematic view of the soft x-ray scattering geometry with $\vec{k}$ and $\vec{k}'$ denoting the wave vectors of incident and scattered photons, respectively.

in the scattering plane. The angle between the [001] axis and the scattering plane is denoted as ϕ.

5.2.4 Incommensurate AFM Order above the Neel Temperature

Figure 5.18(A) is the contour plot of the scattering from LSMO with momentum transfer $\vec{q}$ in the plane defined by the momentum transfer along the [001] and [110] directions denoted as $q_{001}(q_z)$ and q_{110}, respectively. Obviously, the highest scattering intensity is (1/4, 1/4, 1/2) due to 3D AFM order. To enhance the contour plot of low-intensity scattering, we truncate the contour plot of $\vec{q}$ around (1/4, 1/4, 1/2). The contour plot also contains a local maximum at (1/4, 1/4, 0) resulting from the charge orbital ordering. Because of the two-dimensional character of the MnO_2 plane, the contour plot exhibits a long tail along the q_z direction. The q_z and q_{110} momentum
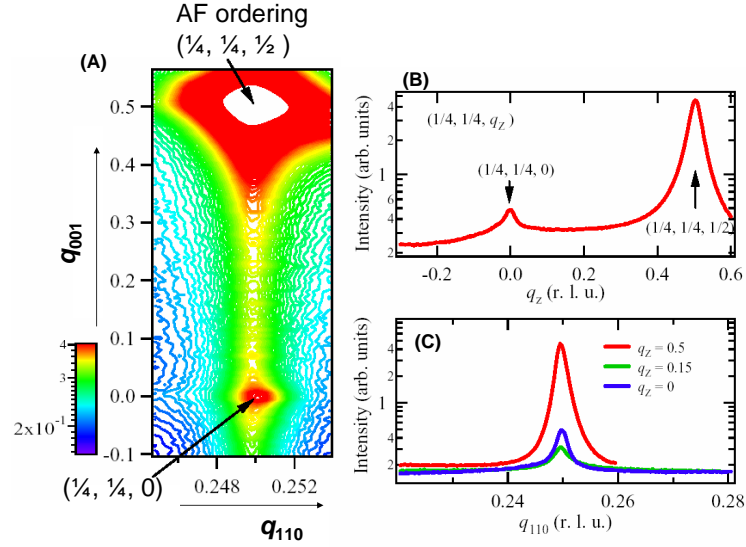
Figure 5.18: (A)Intensity contour of Mn L-edge resonant scattering from LSMO plotted in the plane defined by q_{110} and q_z at 100 K with photon energy of 639 eV. (B) and (C): Momentum scans of Mn L-edge resonant scattering from LSMO with scan of momentum transfer q along the [001] and [110] directions.

scans plotted in Fig. 5.18(B) and 5.18(C) clearly reveal the stripe-like feature along the [001] direction, as a consequence of the anisotropic layered structure. For example, the q_{110} scan with $q_z = 0.15$ shows a well defined peak at $q_{110} = 0.25$, whereas the q_z scan with $q_{110} = 0.25$ is featureless at $q_z = 0.15$. In addition, the intensity of (1/4, 1/4, 1/2) 3D AFM order decreases by increasing temperature, as shown in Fig 5.19(A). The Neel temperature is 113 K. However, above Neel temperature as shown in the inset of Fig 5.19(A), the scattering intensity of 3D AFM order does not go to zero completely. We scanned along the q_{110} and q_{001} direction above Neel temperature. The inset of Fig 5.19(B) shows the q_z scan with q_{110} fixed at 0.25 and the q_{110} scan with q_z fixed at 0.5 for $T = 120$ K. We also found the anisotropy in q dependence. Along in-plane q_{110} direction, the peak is well-defined. But along out-of plane q_{001}

direction, the line-shape is quite flat. These scans reveal that spins in adjacent MnO_2 planes are completely uncorrelated for temperatures above T_N. It shows that this scattering signal is out of 2D order. A question naturally arises: does this 2D order belong to charge-orbital order or magnetic order?
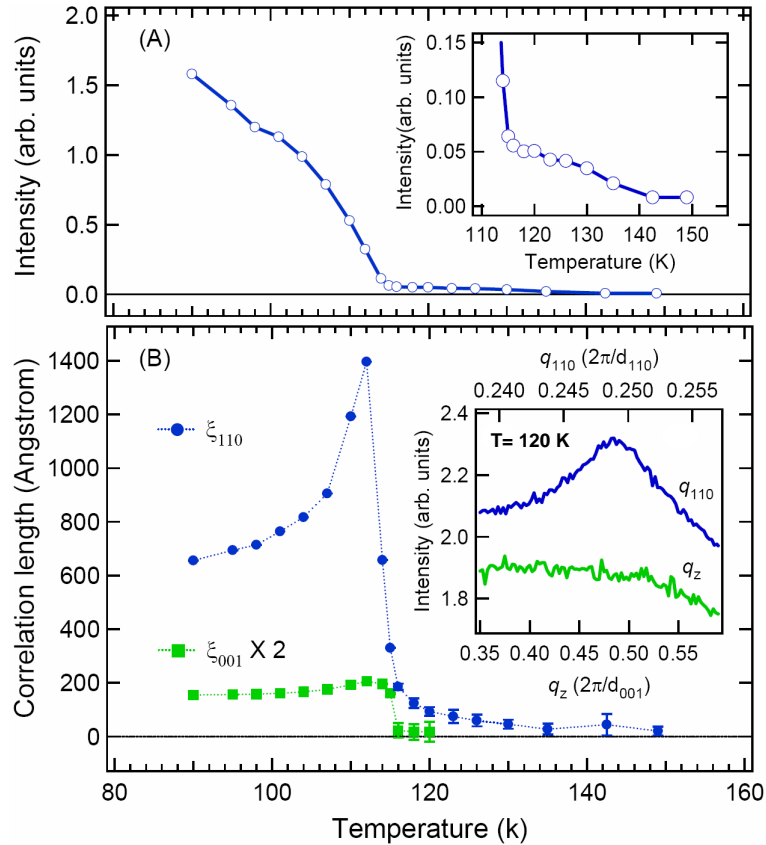
Figure 5.19: Temperature dependence of (1/4, 1/4, 1/2) 3D AFM order. (A)Plot of scattering intensity versus temperature. Inset: Scattering intensity above Neel temperature. (B) Plot of correlation length versus temperature. Inset: q_{110} and q_{001} scans at 120 K with vertical offsets for clarity.

To further examine the AFM nature of the observed residual intensity at temperatures above T_N, we measured resonant scattering with the azimuthal angle $\phi = 90°$, in which the orbital order of (1/4, 1/4, 0) makes no contribution to scattering, because of

its $\cos^2 \phi$ dependence [84]. We observed a finite scattering intensity of $\vec{q} = (1/4, 1/4, 0)$ with $\phi = 90°$; the HWHM of the q_{110} scan is nearly identical to that of the $(1/4, 1/4, 1/2)$ scattering. In addition, the energy dependence of such scattering, as in the curve (C) of Fig. 5.20, resembles closely to those of the measured $(1/4, 1/4, 1/2)$ scattering and calculations [84, 66], in sharp contrast to that from orbital order depicted in the curve (D) of Fig. 5.20. The measured $(1/4, 1/4, q_z)$ scattering above T_N indeed arises from AFM order, and hence our measurements unambiguously show the existence of 2D AFM order for $T > T_N$.
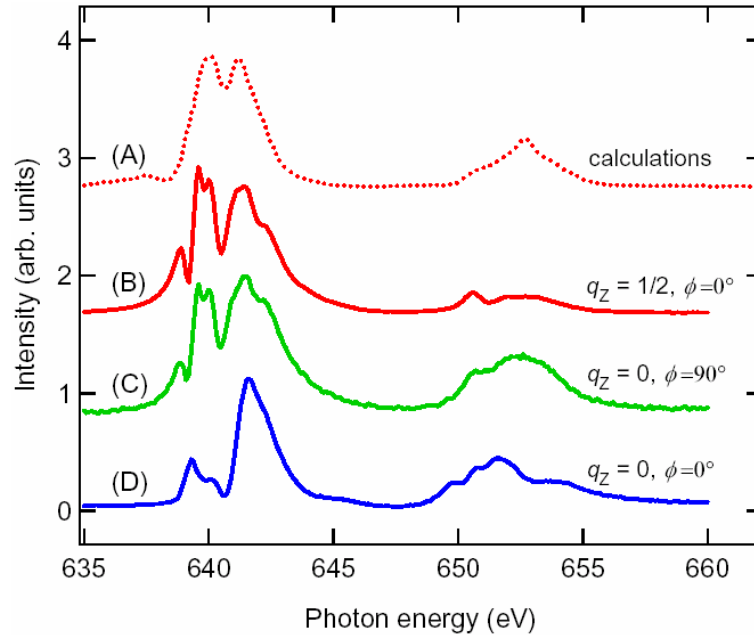
Figure 5.20: Plot of soft x-ray scattering intensity of LSMO with $q = (1/4, 1/4, q_Z)$ versus photon energy around Mn L-edge absorption (A)Calculated spectrum was reproduced from Wilkins *et al.* [84]. (B) Measurement out of 3D AFM order at 100 K. (C) Measurement out of 2D AFM order at 140 K (above Neel temperature). (D) Measurement out of charge-orbital order at 100 K.

The q scans were fitted to a Lorentzian function with a quadratic background to determine the half-width at half maxima (HWHM). The in-plane ξ defined as

the inverse of the HWHM was obtained by subtracting the intrinsic width of 0.002 Ådue to the instrumental resolution and the penetration depth of photon. Figure 5.19(B) plots the temperature dependence of spin correlation lengths ξ_{110} and ξ_{001} along the [110] and [001] directions. When the temperature cools down from a high temperature, the correlation length exponentially increases and shows a cusp feature in its temperature dependence at T_N. The detailed fitting to ξ_{110} is shown in Fig. 5.21. For $T > 120$ K, ξ_{110} shows an exponential decrease in inverse temperature, following the expression.

$$\xi_{110}/a \sim \xi_0 e^{2\pi(S+1)SJ/k_BT}, \tag{5.1}$$

By using $S = 3/2$, we found that $\xi_0 \sim 0.014$ and the average in-plane exchange coupling constant J of LSMO is ~ 3.2 meV, close to the J value of 3.4 meV of LaSrMnO$_4$ reported in measurements of inelastic neutron scattering [89]. The successful fitting indicates the semi-classical nature of 2D AFM order in this temperature regime. Between 120 K and T_N, ξ_{110} starts to deviate from the 2D semi-classical behavior and shows clear enhancement with a power-law behavior:

$$\xi_{110}/a \propto (\frac{T}{T_N} - 1)^{-\nu}, \tag{5.2}$$

Although the number of data points is not sufficient for precisely determining the critical exponent ν, the observed enhancement in spin correlation reflects the critical fluctuations due to the 3D AFM transition, which nonetheless has never been directly observed in neutron measurements on cuprates [94].
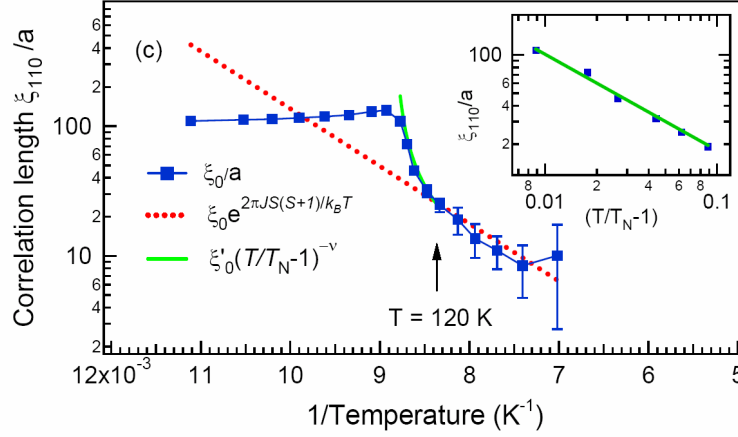
Figure 5.21: Plot of correlation length with log scale versus 1/T.

5.2.5 Incommensurate-to-Commensurate AFM Transition

In addition to exhibiting the critical behavior of correlation length, we also found 2D AFM order is incommensurate above Neel temperature. The system exhibits a remarkable lock-in transition on top of the dimensional crossover transition. As shown in Fig. 5.22(A), the peak of q_{110} scan is shift away 0.25 above T_N. The vertical black dashed line is guide for eye. But below T_N, the incommensurability disappear. As we seen in Fig. 5.22(B), there exists a clear change in q_{110} when temperature crosses T_N, while the change of the ordering wavevector along [-110], i.e., q_{-110}, only responds to the orthorhombicity of lattice as shown black dotted line [89]. The observed change of q_{110} is much larger than what caused by the thermal expansion of lattice [88], indicating a lock-in transition at T_N. Theoretical result suggests that the existence of incommensurability comes from competition between nearest-neighbor zigzag chain and next-nearest-neighbor zigzag chain. When the interlayer coupling overcomes thermal fluctuation, the incommensurability disappears [96].
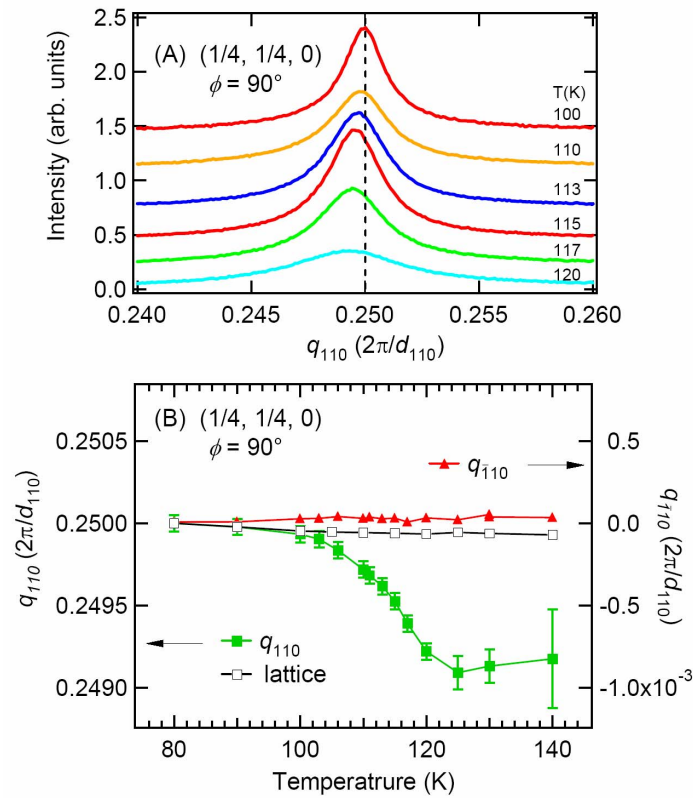
Figure 5.22: (A) Graphs of in-plane AFM order at 100 K, 110K, 113 K, 115 K, 117 K, and 120 K, respectively. All graphs were vertical offset for clarity. Black line is guide for eye. (B) Temperature dependence of modulation vector of (1/4, 1/4, 0) AFM order along q_{110} (Green) and q_{-110} (Red) direction. Black dotted line is plot of lattice changes versus temperature.

Based on experiments of resonant soft-x-ray scattering, we investigate the antiferromagnetic transition in a CE-type antiferromagnet LSMO. We disclose the critical behavior in a CE-type antiferromagnet which evolves from quasi-2D semi-classical AFM to 3D AFM order as the temperature cools across T_N. Quasi-2D incommensurate AFM order prevails at temperatures above the Neel temperature. As the temperature cools across T_N, on top of the dimensional crossover, the 2D incommensurate AFM order collapses to stabilize the 3D commensurate AFM order showing a lock-in transition. Our results show that the spin correlation follows the same exponential growth in inverse temperature as those observed in quantum Heisenberg antiferromagnets.

Chapter 6

Conclusions

We developed an experimental technique of resonant soft-x-ray scattering employing the EPU beamline and a UHV two-circle diffractometer. With this technique, we investigated spin, charge, and orbital ordering of novel transition-metal oxides in connection with their fascinating macroscopic physical properties. Our results unravel the underlying physics of the Verwey transition of magnetite, a classical issue on charge ordering. We also studied the symmetry of multiferroicity in a frustrated magnet $TbMn_2O_5$. The third subject is on magnetic and charge-orbital transition of single-layered manganites.

In our viewpoint, the newly established scattering technique opens an avenue for exploring subtle and diverse effects arising from the ordering of electronic states. Scientific subjects discussed in this dissertation, such as magnetic phase transitions and multiferroicity, are in the frontier of current research in condensed matter physics.

One could further anticipate new phenomena of emergent materials revealed by resonant soft-x-ray scattering.

Reference

[1] Y. Tokura and N. Nagaosa, Science **288**, 462 (2000).

[2] M. Imada, A. Fujimori, and Y. Tokura, Rev. Mod. Phys. **70**, 1039 (1998).

[3] C. H. Chen and S-W. Cheong, Phys. Rev. Lett. **76**, 4042 (1996).

[4] Yoshinori Tokura, Science **312**, 1481 (2006).

[5] W. Eerenstein, N. D. Mathur, J. F. Scott, Nature **442**, 759 (2006).

[6] J.P. Hill, C.S. Nelson, M. v. Zimmermann, Y.-J.Kim, D. Gibbs, D. Casa, B.Keimer, Y. Murakami, C. Venkataraman, T.Gog, Y. Tomioka, Y. Tokura, V. Kiryukhin, T.Y.Koo, and S.-W.Cheong, Appl. Phys. A **73**, 723V730 (2001)

[7] For example, Y. Tokura, Ed., Colossal Magnetoresistive Oxides (Gordon and Breach Science, New York, 2000).

[8] E. Dagotto, T. Hotta, and A. Moreo, Proc. Physics Report **344**, 1-153 (2001).

[9] N. F. Mott, Proc. Phys. Soc. London Sect. A**62**, 416 (1949).

[10] C. Zener, Phys. Rev. **81**, 440 (1951); Phys. Rev. **82**, 403 (1951); Phys. Rev. **83**, 299 (1951)

[11] E.O. Wollan, W.C. Koehler, Phys. Rev. **100**, 545. (1955)

[12] J. B. Goodenough, Phys. Rev. **100**, 564 (1955).

[13] M. Blume, J. Appl. Phys. **57**, 3615 (1985).

[14] C. G. Shull and J. S. Smart, Phys. Rev. **76**, 1256 (1949).

[15] J. M. Tranquada, H. Woo, T. G. Perring, H. Goka, G. D. Gu, G. Xu, M. Fujita, K. Yamada, Nature **429**, 534 - 538 (2004).

[16] W. C. Koehler, J. W. Cable, M. K. Wilkinson, and E. O. Wollan, Phys. Rev. **151**, 414. (1966)

[17] Doon Gibbs, D. R. Harshman, E. D. Isaacs, and D. B. McWhan, D. Mills, C. Vettier, Phys. Rev. Lett. **61**, 1241 (1988).

[18] J. P. Hannon, G. T. Trammell, M. Blume, D. Gibbs, Phys. Rev. Lett. **61**, 1241 (1988).

[19] Y. Murakami H. Kawada, H. Kawata, M. Tanaka, T. Arima, Y. Moritomo, Y. Tokura, Phys. Rev. Lett. **80**, 1932 (1998).

[20] S. B. Wilkins, P. D. Hatton, M. D. Roper, D. Prabhakaran, A. T. Boothroyd, Phys. Rev. Lett. **90**, 187201 (2003).

[21] P. Abbamonte, L. Venema, A. Rusydi, G. A. Sawatzky, G. Logvenov, and I. Bozovic, Science **297**, 581 (2002).

[22] P. Abbamonte, G. Blumberg, A. Rusydi, A. Gozar, P.G. Evans, T. Siegrist, L. Venema, H. Eisaki, E. D. Isaacs, and G. A. Sawatzky, Nature **431**, 1078 (2004).

[23] K. J. Thomas, J. P. Hill, S. Grenier, Y.-J. Kim, P. Abbamonte, L. Venema, A. Rusydi, Y. Tomioka, Y. Tokura, D. F. McMorrow, G. Sawatzky, and M. van Veenendaal, Phys. Rev. Lett. **92**, 237204 (2004).

[24] C. W. M. Castleton, M. Altarelli, Phys. Rev. B **62**, 1033 (2000).

[25] S.-C. Chung, Y.-F. Song, P.-C. Tseng, C.-C. Chen, C. T. Chen and K.-L. Tsang, J. Synchrotron Rad., **5**, 551-553 (1998)

[26] S.-C. Chung, J. Chen, L.-R. Huang, R.T. Wu, C.-C. Chen, N.-F. Cheng, J.M. Chuang, P.-C. Tseng, D.J. Huang, C.F. Chang, S.-Y. Perng, C.T. Chen, K.-L. Tsang, Nucl. Instr. and Meth. A, **467-468**, 445-448 (2001)

[27] S. Sasaki, Nucl. Instr. and Meth. A, **347**, 83 (1994)

[28] For review on the research of the Verwey transition, see F. Walz, J. Phys. Condens. Matter, Science **14**, R285 (2002); J. Garcia and G. Subias, J. Phys. Condens. Matter, Science **16**, R145 (2004)

[29] E. J.W. Verwey and P.W. Haayman, Physica (Amsterdam) **8**, 979 (1941).

[30] F. Mott, Philos. Mag. B **42**, 327 (1980).

[31] Y. Yamada, Philos. Mag. B **42**, 377 (1980).

[32] A. Yanase and N. Hamada, J. Phys. Soc. Jpn. **68**, 1607 (1999).

[33] J. P. Wright, J. P. Attfield, and P. G. Radaelli, Phys. Rev. Lett. **87**, 266401 (2001).

[34] J. P. Wright, J. P. Attfield, and P. G. Radaelli, Phys. Rev. B **66**, 214422 (2002).

[35] I. Leonov, A.N. Yaresko, V. N. Antonov, M.A. Korotin, and V. I. Anisimov, Phys. Rev. Lett. **93**, 146404 (2004).

[36] H. T. Jeng, G.Y. Guo, and D. J. Huang, Phys. Rev. Lett. **93**, 156403 (2004).

[37] G. Subias, J. Garcia, J. Blasco, M. Grazia Proietti, H. Renevier, and M. C. Sanchez, Phys. Rev. Lett. **93**, 156408 (2004).

[38] K. Siratori, Y. Shii, Y. Morii, S. Funahashi, S. Todo, and A. Yanase, J. Phys. Soc. Jpn. **67**, 2818 (2000).

[39] P. Novak, H. Stepankova, J. Englich, J. Kohout, and V. A. M. Brabers, Phys. Rev. B **61**, 1256 (2000).

[40] J. Garcia, G. Subias, M. G. Proietti, H. Renevier, Y. Joly, J. L. Hodeau, J. Blasco, M. C. Sanchez, and J. F. Berar, Phys. Rev. Lett. **85**, 578 (2000).

[41] J. Garcia, G. Subias, M. G. Proietti, J. Blasco, H. Renevier, J. L. Hodeau, and Y. Joly, Phys. Rev. B **63**, 054110 (2001).

[42] M. Takahashi, M. Usuda, and J. Igarashi, Phys. Rev. B **67**, 064425 (2003).

[43] N. Binggeli and M. Altarelli, Phys. Rev. B **70**, 085117 (2004).

[44] G.Y. Guo *et al.* (to be published).

[45] A. Chainani, T. Yokoya, T. Morimoto, T. Takahashi, and S. Todo, Phys. Rev. B **51**, 17976 (1995).

[46] S. K. Park, T. Ishikawa, and Y. Tokura, Phys. Rev. B **58**, 3717 (1998).

[47] P. Curie, J. Physique **3**, 393 (1894).

[48] M. Fiebig, J. Phys. D: Appl. Phys. **38**, R123 (2005).

[49] T. Kimura, T. Goto, H. Shintani, K. Ishizaka, T. Arima, Y. Tokura, Nature **426**, 55 (2003).

[50] N. Hur, S. Park, P. A. Sharma, J. S. Ahn, S. Guha, S-W. Cheong Nature **429**, 392 (2004).

[51] N. Hur, S. Park, P. A. Sharma, S. Guha, S-W. Cheong, Phys. Rev. Lett. **93**, 107207 (2004).

[52] D. Higashiyama, S. Miyasaka, N, Kida, T. Arima, Y. Tokura, Phys. Rev. B **70**, 174405 (2004).

[53] Satoru Kobayashi, Toshihiro Osawa, Hiroyuki Kimura, Yukio Noda, Noriaki Kasahara, Setsuo Mitsuda, Kay Kohn, J. Phys. Soc. Jpn. **73**, 3439 (2004).

[54] L. C. Chapon, G. R. Blake, M. J. Gutmann, S. Park, N. Hur, P.G. Radaelli, S-W. Cheong, Phys. Rev. Lett. **93**, 177402 (2004).

[55] G. R. Blake, L. C. Chapon, P. G. Radaelli, S. Park, N. Hur, S-W. Cheong, J. Rodríguez-Carvajal, Phys. Rev. B **71**, 214402 (2005).

[56] D. Higashiyama, S. Miyasaka, Y. Tokura, Phys. Rev. B **72**, 64421 (2005).

[57] M. Kenzelmann, A. B. Harris, S. Jonas, C. Broholm, J. Schefer, S. B. Kim, C. L. Zhang, S-W. Cheong, O. P. Vajk, J.W. Lynn, Phys. Rev. Lett. **95**, 087206 (2005).

[58] T. Arima, A. Tokunaga, T. Goto, H. Kimura, Y. Noda, Y. Tokura, Phys. Rev. Lett. **96**, 097202 (2006).

[59] L. C. Chapon, P. G. Radaelli, G. R. Blake, S. Park, S-W. Cheong, Phys. Rev. Lett. **96**, 97201 (2006).

[60] D. V. Efremov, J. van den Brink, D. I. Khomskii, Nature Mater. **3**, 853 (2004).

[61] H. Katsura, N. Nagaosa, A. V. Balatsky, Phys. Rev. Lett. **95**, 57205 (2005).

[62] I. A. Sergienko and E. Gagotto, Phys. Rev. B **73**, 094434 (2006).

[63] C. G. Shull, W. A. Strauser, and E. O. Wollan, Phys. Rev. **83**, 333 (1951).

[64] G. Lawes, A. P. Ramirez, C. M. Varma, M. A. Subramanian, Phys. Rev. Lett. **91**, 257208 (2003).

[65] M. Mostovoy, Phys. Rev. Lett. **96**, 067601 (2006).

[66] N. Stojić, N. Binggeli, M. Altarelli, Phys. Rev. B **72**, 104108 (2005).

[67] J. Okamoto, D. J. Huang, C.-Y. Mou, K. S. Chao, H.-J. Lin, S. Park, S-W. Cheong, and C. T. Chen, Phys. Rev. Lett. **98**, 157202 (2007).

[68] J. B. Torrance, P. Lacorre, A. I. Nazzal, E. J. Ansaldo, and Ch. Niedermayer, Phys. Rev. B. **45**, 8209 (1992).

[69] J. P. Attfield, Chem. Mater. **10**, 3239-3248 (1998).

[70] R. Mathieu, M. Uchida, Y. Kaneko, J. P. He, X. Z. Yu, R. Kumai, T. Arima, Y. Tomioka, A. Asamitsu, Y. Matsui and Y. Tokura, Phys. Rev. B **74**, 020404 (2006).

[71] Y. Moritomo, Y. Tomioka, A. Asamitsu, Y. Tokura, and Y. Matsui, Phys. Rev. B **51**, 3297 (1995).

[72] W. Bao, C. H. Chen, S.-W. Cheong, S. A. Carter, Solid State Commun. **98**, 55 (1996).

[73] P.-G. de Gennes, Phys. Rev. **118**, 141 (1960).

[74] See, for example, M. A. Kastner, R. J. Birgeneau, G. Shirane, and Y. Endoh, Rev. Mod. Phys. **70**, 897 (1998).

[75] N. D. Mermin and H. Wagner, Phys. Rev. Lett. **17**, 1133 (1966).

[76] S, Chakravarty, B. I. Halperin, and D. R. Nelson, Phys. Rev. Lett. **60**, 1057 (1988); Phys. Rev. B **39**, 2344 (1989).

[77] M. Greven, R. J. Birgeneau, Y. Endoh, M. A. Kastner, B. Keimer, M. Matsuda, G. Shirane, and T. R. Thurston, Phys. Rev. Lett. **72**, 1096 (1994).

[78] O. P. Vajk, P. K. Mang, M. Greven, P. M. Gehring, and J.W. Lynn, Science **295**, 1691 (2002).

[79] N. Elstner A. Stokol, R.R.P. Singh, M. Greven, and R. J. Birgeneau, Phys. Rev. Lett. **75**, 938 (1995).

[80] A. Cuccoli, V. Tognetti, R. Vaia, and P. Verrucchi, Phys. Rev. Lett. **77**, 3439 (1996).

[81] R. L. Leheny, R. J. Christianson, R. J. Birgeneau, and R. W. Erwin, Phys. Rev. Lett. **82**, 418 (1999).

[82] B. J. Sternlieb, J. P. Hill, U. C. Wildgruber, G. M. Luke, B. Nachumi, Y. Moritomo, Y. Tokura, Phys. Rev. Lett. **76**, 2169 (1996).

[83] D. Senff and F. Kruger and S. Scheidl and M. Benomar and Y. Sidis and F. Demmel and M. Braden, Phys. Rev. Lett. **96**, 257201 (2006).

[84] S. B. Wilkins, N. Stojić, T. A. W. Beale, N. Binggeli, C. W. M. Castleton, P. Bencok, D. Prabhakaran, A. T. Boothroyd, P. D. Hatton, and M. Altarelli, Phys. Rev. B **71**, 245102 (2005).

[85] U. Staub, V. Scagnoli, A. M. Mulders, K. Katsumata, Z. Honda, H. Grimmer, M. Horisberger, J. M. Tonnerre, Phys. Rev. B **72**, 214421 (2005).

[86] U. Staub, V. Scagnoli, A. M. Mulders, M. Janousch, Z. Honda and J. M. Tonnerre, Europhysics Lett. **76**, 926 (2006).

[87] M. Tokunaga, N. Miura, Y. Moritomo, Y. Tokura, Phys. Rev. B **59**, 11151 (1999).

[88] D. Senff, P. Reutler, M. Braden, O. Friedt, D. Bruns, A. Cousson, F. Bourée, M. Merz, B. Büchner, and A. Revcolevschi, Phys. Rev. B **71**, 024425 (2005).

[89] S. Larochelle, A. Mehta, L. Lu, P. K. Mang, O. P. Vajk, N. Kaneko, J. W. Lynn, L. Zhou, M. Greven, Phys. Rev. B **71**, 024435 (2005).

[90] Chang Seop Hong, Wan Seop Kim, Nam Hwi Hur, and Yong Nam Choi, Phys. Rev. B **68**, 64425 (2003).

[91] Y. Moritomo, A. Nakamura, S. Mori, N. Yamamoto, K. Ohoyama, M. Ohashi Phys. Rev. B **56**, 14879 (1997).

[92] D. J. Huang, W. B. Wu, G. Y. Guo, H.-J. Lin, T. Y. Hou, C. F. Chang, C. T. Chen, A. Fujimori, T. Kimura, H. B. Huang, A. Tanaka, T. Jo, Phys. Rev. Lett. **92**, 87202 (2004).

[93] S. B. Wilkins, P. D. Hatton, and M. D. Roper, Phys. Rev. Lett. **91**, 167205 (2003).

[94] See, for example, B. Keimer *et al.*, Phys. Rev. B **46**, 14034 (1992). The critical behavior for cuprates was indirectly measured with nuclear magnetic resonance in F. Borsa *et al.*, Phys. Rev. B **45**, 5756 (1992).

[95] R. Mathieu *et al.*, unpublished.

[96] K. S. Chao *et al.*, submitted

Appendix A

Comparison of Magnetic Soft X-Ray and Neutron Scattering

In this thesis, we discussed resonant soft-x-ray magnetic scattering to probe magnetic order. More than 50 years, neutron scattering have been demonstrated to be one of the best techniques to probe magnetic order. Here we compare these two techniques.

- The cross-section of magnetic neutron scattering is larger than that of soft-x-ray scattering by a factor of 10^6. By using a resonance effect, the cross-section of resonant soft-x-ray scattering can be enhanced by a factor of 10^2. In addition, the flux of soft x-rays from synchrotron radiation is around 10^{12} photons larger than that of neutron by a factor of 10^4., the flux of x-ray is larger than that of neutron scattering by the factor 10^4. Hence measurements of resonant magnetic soft-x-ray scattering and neutron scattering have a comparable efficiency.

- The neutron is neutral and can penetrate deeply into materials, providing informations on the bulk properties. For resonant soft-x-ray scattering, the penetration depth is in the order of around 1000 Å.

- The soft x-ray can be focused into a small spot with 100*100 μm beam size on samples. Therefore for soft-x-ray scattering measurements do not require large sample sizes.

- Measurements of neutron scattering can access a large momentum transfer, while the momentum transfer reached by soft-x-ray scattering is smaller than 1 Å^{-1}. Due to the long wavelength of soft-x-ray, Only the small momentum transfer is accessible.

- The measurement of soft x-ray scattering can provide higher q resolution than that of neutrons. In fact, our measurements of TbMn$_2$O$_5$ and LSMO samples show higher q resolution than that with neutrons.

- The x-ray magnetic scattering provides an element-specific probe. Because the magnetic ordering arises from the $3d$ band of transition-metals, the soft-x-ray scattering can probe magnetic orderings directly and with high sensitivity.

Appendix B

List of Publications

- D. J. Huang, H.-J. Lin, J. Okamoto, K. S. Chao, H. -T Jeng, G. Y. Guo, C. -H. Hsu, C. -M Huang, D. C. Ling, W. B. Wu, C. S. Yang, and C. T. Chen, "Charge-Orbital Ordering and Verwey Transition in Magnetite Measured by Resonant Soft X-ray Scattering", Phys. Rev. Lett. **96**, 096401 (2006).

- K. S. Chao, D. J. Huang, H.-J. Lin, J. Okamoto, C. -H. Hsu, C. -M Huang, W. B. Wu, and C. T. Chen, "Charge-Orbital Ordering of Magnetite Studied by Soft Resonant X-ray Scattering", Physica B **378-380**, 565 (2006).

- K. S. Chao, D. J. Huang, J. Okamoto, H.-J. Lin, C.-H. Hsu, Y. Kaneko, R. Mathieu, W.B. Wu, Y. Tokura, and C. T. Chen, "Orbital ordering of layered manganites from resonant soft X-ray scattering", J. Magn. Magn. Mater., **310**, 819-821 (2007).

- J. Okamoto, D. J. Huang, C.-Y. Mou, K. S. Chao, H.-J. Lin, S. Park, S-W. Cheong, and C. T. Chen, "Symmetry of Multiferroicity in a Frustrated Magnet

TbMn$_2$O$_5$", Phys. Rev. Lett. **98**, 157202 (2007).

- K. S. Chao, D. J. Huang, J. Okamoto, C.-Y. Mou, H.-J. Lin, C.-H. Hsu, Y. Kaneko, R. Mathieu, Y. Tokura, C. H. Chen, and C. T. Chen, "Quasi-Two-Dimensional Antiferromagnetic Order in La$_{0.5}$Sr$_{1.5}$MnO$_4$ Investigated by Soft X-ray Magnetic Scattering", submitted to PRL (2006).